

Assessing the potential of Jacobian-free Newton-Krylov methods for cell-centred finite volume solid mechanics

Philip Cardiff^{1,2,3*}, Ivan Batistić⁴ and Željko Tuković⁴

¹*School of Mechanical and Materials Engineering, University College Dublin, Ireland.

²UCD Centre for Mechanics, University College Dublin, Ireland.

³SFI I-Form Centre, University College Dublin, Ireland.

⁴Faculty of Mechanical Engineering and Naval Architecture, University of Zagreb, Croatia.

*Corresponding author. E-mail: philip.cardiff@ucd.ie

Abstract

In this study, we explore the efficacy of Jacobian-free Newton-Krylov methods within the context of finite-volume solid mechanics. Traditional Newton-based approaches to solving nonlinear systems typically require explicit formation and storage of the Jacobian matrix, which can be computationally expensive and memory-intensive. The Jacobian-free Newton-Krylov method circumvents this by employing Krylov subspace iterative solvers, such as GMRES, in conjunction with a Newton iteration scheme that approximates the action of the Jacobian through finite difference evaluations. A further potential advantage of the Jacobian-free Newton-Krylov method is that it is readily applicable to existing segregated finite volume frameworks, where forming and storing the exact Jacobian would require major code refactoring. This article research systematically evaluates the performance of Jacobian-free Newton-Krylov methods by benchmarking them against conventional segregated methods on a suite of benchmark cases of varying geometric dimension, geometric nonlinearity, dynamic response, and material behaviour. Key metrics such as computational cost, memory and robustness are analysed. Additionally, we investigate the impact of various solution algorithm choices, such as preconditioning strategy, on the efficiency of the Jacobian-free Newton-Krylov method. Our findings indicate that Jacobian-free Newton-Krylov methods can achieve comparable/superior/XXX convergence behaviour relative to traditional segregated methods, particularly in cases where YYYY. Summarise key findings: time, memory, important choices, JFNK vs SEG vs FE, ... The results suggest that Jacobian-free Newton-Krylov methods are promising for advancing finite-volume solid mechanics simulations and are particularly attractive for existing segregated frameworks where minimal code changes would be required to exploit openly available Jacobian-free Newton-Krylov implementations. The described implementations are made publicly available in the solids4foam toolbox for OpenFOAM, allowing the community to examine, extend and compare the procedures with the our codes.

1 Introduction

Finite volume formulations for solid mechanics are heavily influenced by their fluid mechanics counterparts, favouring fully explicit [1–4] or segregated implicit [5–12] methods. Segregated approaches, where the governing momentum equation is temporarily decomposed into scalar component equations, offer memory efficiency and simplicity of implementation, but the outer coupling Picard iterations often suffer from slow convergence. Explicit formulations are straightforward to implement and offer superior robustness but are only efficient for high-speed dynamics, where the physics requires small time increments. In contrast, the finite element community commonly employs Newton-Raphson-type solution algorithms, which necessitate repeated assembly of the Jacobian matrix and solution of the resulting block-coupled non-diagonally dominant linear system. A disadvantage of traditional Newton-based approaches is that they typically require explicit formation and storage of the Jacobian matrix, which can be computationally expensive and memory-intensive. A further disadvantage from a finite volume perspective is that extending existing code frameworks from segregated algorithms to coupled Newton-Raphson-type approaches is challenging in terms of the required assembly, storage, and solution of the resulting block-coupled system. In addition, the derivation of the true Jacobian matrix is non-trivial. Consequently, similar block-coupled solution finite volume methods are rare in the literature [13–15]. The motivation of the current work is to seek (or exceed) the robustness and efficiency of block-coupled Newton-Raphson approaches in a way that can be easily incorporated into existing segregated solution frameworks. To this end, the current article examines the efficacy of *Jacobian-free* Newton-Krylov methods, where the quadratic convergence of Newton methods can potentially be achieved without deriving, assembling and storing the exact Jacobian.

Jacobian-free Newton-Krylov methods circumvent the need for the Jacobian matrix by combining the Newton-Raphson method with Krylov subspace iterative linear solvers, such as GMRES, and noticing that such Krylov solvers do not explicitly require the Jacobian matrix. Instead, only the action of the Jacobian matrix on a solution-type vector is required. The key step in Jacobian-free Newton-Krylov methods is the approximation of products between the Jacobian matrix and a vector using the finite difference method; that is

$$\mathbf{J}\mathbf{v} \approx \frac{\mathbf{F}(\mathbf{x} + \epsilon\mathbf{v}) - \mathbf{F}(\mathbf{x})}{\epsilon} \quad (1)$$

where \mathbf{J} is the Jacobian matrix, \mathbf{x} is the current solution vector (e.g. nodal displacements), \mathbf{v} is a vector (e.g., from a Krylov subspace), and ϵ is a small scalar perturbation. With an appropriate choice of ϵ (balancing truncation and round-off errors), the characteristic quadratic convergence of Newton methods can be achieved without the Jacobian, hence the modifier *Jacobian-free*. This approach promises significant memory savings over Jacobian-based methods, especially for large-scale problems, but also potentially for execution time, with appropriate choice of solution components.

A crucial aspect of ensuring the efficiency and robustness of the Jacobian-free Newton-Krylov method is the choice of a suitable preconditioner for the Krylov iterations. This preconditioner is often derived from the exact Jacobian matrix in traditional Newton methods. However, the Jacobian-free approach does not allow direct access to the full Jacobian matrix, necessitating an alternative strategy to approximate its action. To this end, and to extend existing segregated frameworks, this work proposes using a compact-stencil *approximate* Jacobian as the preconditioner. This approximate Jacobian corresponds to the matrix typically employed in segregated solid mechanics approaches; similar approaches are successful in fluid mechanics applications [16–25]; however, it is unclear if such an approach is suitable for solid mechanics - a question this work aims to answer. By leveraging this compact-stencil approximate Jacobian, it is aimed to effectively precondition the Krylov iterations, enhancing convergence while maintaining the memory and computational savings that define the Jacobian-free and segregated methods. Similarly, if such an approach is efficient, it would naturally fit into existing segregated frameworks, as existing matrix storage and assembly can be reused.

As noted by Knoll and Keyes [20], Jacobian-Free Newton–Krylov methods first appeared in the 1980s and early 1990s for the solution of ordinary and partial differential equations [26–29]. McHugh and Knoll [16] and co-workers demonstrated the potential of Jacobian-free Newton-Krylov approaches for the solution of steady, incompressible, Navier-Stokes problems using a staggered finite volume formulation. They found the GMRES linear solver to be faster than a conjugate solver, however, the true Jacobian matrix was still evaluated by finite differencing in the construction of the preconditioning matrix. Qin et al. [17] later extended Jacobian-Free Newton–Krylov methods to unsteady compressible Reynolds-averaged Navier–Stokes equations. Once again it was found that GMRES was more robust than a conjugate gradient linear solver. For preconditioning, a fully matrix-free approach was proposed, based on the approximate factorization procedure of Badcock and Gaitonde [30]. Geuzaine [18] examined the use of lower and higher-order discretisations for the preconditioning matrix for steady, compressible high Reynolds number flows. They found that the lower-order compact stencil preconditioner gave the best performance when combined with the GMRES linear solver and ILU(k) preconditioner. As is common with other Newton approaches, a pseudo transient algorithm and mesh sequencing strategy were used to improve the convergence. With the aim of exploiting mature segregated solution approaches, Pernice and Tocci [19] recast the SIMPLE segregated algorithm as a method which operators on residuals, allowing it to act as the preconditioner for a Jacobian-free Newton-Krylov approach. It was found that the SIMPLE-preconditioned Jacobian-free Newton-Krylov substantially accelerated convergence for the incompressible Navier–Stokes problems examined. GMRES was the adopted linear solver, where the importance of choosing an appropriate restart parameter was noted. They also found a multigrid approach to be more efficient than ILU for preconditioning, where the implementation was based on the PETSc [31] package.

Over the subsequent two decades, Jacobian-free Newton-Krylov methods have seen increasing application in the field of finite volume computational fluid dynamics, albeit they are still far from widespread. The use of low-order approximate Jacobians for preconditioning has been established as an efficient and robust approach, e.g. [21, 22, 24, 25]. A particularly attractive application of the low-order-discretisation preconditioned Newton-Krylov is for higher-order discretisations; that is, spatial discretisation of order greater than two. Nejat and Ollivier-Gooch [21] demonstrated such

a higher order approach for steady, inviscid compressible flows, with up to fourth order accuracy. GMRES was the adopted linear solver with the ILU(k) preconditioner and fill-in values (k) ranging from 2 to 4. Nejat et al. [24] later applied the second-order variant of the approach to non-Newtonian flows and found Newton-GMRES with ILU(1) to be the most efficient combination. Like Vaassen et al. [22] and many other authors, Nejat and co-workers [21, 24] proposed a special start-up phase to encourage the solution to efficiently reach the Newton method's domain of quadratic convergence. The use of a pseudo-transient approach combined with an adaptive time step (e.g., based on the convergence of the Newton iterations) is common. A further promotion for the benefit of Jacobian-free Newton-Krylov methods in fluid dynamics was provided by Lucas et al. [23], who demonstrated order of magnitude speedups over nonlinear multigrid methods. A particular benefit was the insensitivity of the Jacobian-free Newton-Krylov methods to changes in mesh aspect ratio, density, time step and Reynolds number. A final relevant point is the effect of numerical stabilisation (damping) on the convergence: Nishikawa et al. [32] demonstrated that a Jacobian-free Newton-Krylov approach was less sensitive to the magnitude of the damping and remained stable for lower values of damping compared with a segregated approach.

Although they are increasingly seen in finite volume computational fluid dynamics, Jacobian-free Newton-Krylov methods have yet to be used for finite volume solid mechanics. This article aims to address this point by assessing the efficacy of Jacobian-free Newton-Krylov cell-centred finite volume formulations applied to static, dynamic, linear and nonlinear solid mechanics problems. Particular focus is given to the use of a compact-stencil approximate Jacobian preconditioner, inspired from existing segregated solid mechanics procedures, and ease of implementation into an existing segregated finite volume framework – OpenFOAM [33]. The remainder of the paper is structured as follows: Section 2 summarises a typical solid mechanics mathematical model and its cell-centred finite volume discretisation. Section 3 presents the solution algorithms, starting with the classic segregated solution algorithm, followed by the proposed Jacobian-free Newton-Krylov solution algorithm. The performance of the proposed Jacobian-free Newton-Krylov approach is compared with the segregated approach on several varying benchmark cases in Section 4, where the effect of several factors are examined, including problem dimension, mesh, material model, nonlinear geometry, choice of preconditioner, and other solution parameter. Finally, the article ends with a summary of the main conclusions of the work.

2 Mathematical Model and Numerical Methods

2.1 Governing Equations

In this work, interest is restricted to Lagrangian formulations of the conservation of linear momentum. Assuming small strains, the linear geometry formulation is expressed in strong integral form as:

$$\int_{\Omega} \rho \frac{\partial^2 \mathbf{u}}{\partial t^2} d\Omega = \oint_{\Gamma} \mathbf{n} \cdot \boldsymbol{\sigma}_s d\Gamma + \int_{\Omega} \mathbf{f}_b d\Omega \quad (2)$$

where Ω is the volume of an arbitrary body bounded by a surface Γ with outwards pointing normal \mathbf{n} . The density is ρ , \mathbf{u} is the displacement vector, $\boldsymbol{\sigma}_s$ is the engineering (small strain) stress tensor, and \mathbf{f}_b is a body force per unit volume, e.g., $\rho\mathbf{g}$, where \mathbf{g} is gravity.

More generally, linear momentum conservation can be expressed in a nonlinear geometry form, which is suitable for finite strains. Two equivalent nonlinear geometry forms are common: the *total* Lagrangian form:

$$\int_{\Omega_o} \rho_o \frac{\partial^2 \mathbf{u}}{\partial t^2} d\Omega_o = \oint_{\Gamma_o} (J \mathbf{F}^{-T} \cdot \mathbf{n}_o) \cdot \boldsymbol{\sigma} d\Gamma_o + \int_{\Omega_o} \mathbf{f}_b d\Omega_o \quad (3)$$

and the *updated* Lagrangian form:

$$\int_{\Omega_u} \frac{\partial}{\partial t} \left(\rho_u \frac{\partial \mathbf{u}}{\partial t} \right) d\Omega_u = \oint_{\Gamma_u} (j \mathbf{f}^{-T} \cdot \mathbf{n}_u) \cdot \boldsymbol{\sigma} d\Gamma_u + \int_{\Omega_u} \mathbf{f}_b d\Omega_u \quad (4)$$

where subscript o indicates quantities in the initial reference configuration, and subscript u indicates quantities in the updated configuration. The true (Cauchy) stress tensor is indicated by $\boldsymbol{\sigma}$. The deformation gradient is defined as $\mathbf{F} = \mathbf{I} + (\nabla \mathbf{u})^T$ and its determinant as $J = \det(\mathbf{F})$. Similarly, the *relative* deformation gradient is given in terms of the displacement *increment* as $\mathbf{f} = \mathbf{I} + [\nabla(\Delta \mathbf{u})]^T$ and its determinant as $j = \det(\mathbf{f})$. The displacement increment is the change in displacement between the current time step and the previous time step when the time interval is discretised into a finite number of steps.

The definition of the engineering stress ($\boldsymbol{\sigma}_s$) and true stress ($\boldsymbol{\sigma}$) in Equations 2, 3 and 4 is given by a chosen mechanical law, e.g. linear elasticity, neo-Hookean hyperelasticity. Several mechanical laws are considered in this work, as briefly described in Section 4.

2.2 Newton-Type Solution Methods

To facilitate the comparison between the classic segregated solution algorithm and the proposed Jacobian-free Newton-Krylov algorithm, the governing linear momentum conservation (Equations 2, 3 and 4) is expressed in the general form:

$$\mathbf{R}(\mathbf{u}) = \mathbf{0} \quad (5)$$

where \mathbf{R} represents the *residual* (imbalance) of the equation, which is a function of the primary unknown field. For example, in the linear geometry case, the residual is given as

$$\mathbf{R}(\mathbf{u}) = \oint_{\Gamma} \mathbf{n} \cdot \boldsymbol{\sigma}_s(\mathbf{u}) d\Gamma + \int_{\Omega} \rho \mathbf{g} d\Omega - \int_{\Omega} \rho \frac{\partial^2 \mathbf{u}}{\partial t^2} d\Omega = \mathbf{0} \quad (6)$$

where the dependence of the stress tensor on the solution vector is made explicitly clear: $\boldsymbol{\sigma}_s(\mathbf{u})$.

In Newton-type methods, a Taylor expansion about a current point \mathbf{u}_k can be used to solve Equation 5 [20]:

$$\mathbf{R}(\mathbf{u}_{k+1}) = \mathbf{R}(\mathbf{u}_k) + \mathbf{R}'(\mathbf{u}_k)(\mathbf{u}_{k+1} - \mathbf{u}_k) + \text{H.O.T.} = \mathbf{0} \quad (7)$$

Neglecting the higher-order terms (H.O.T.) yields the strict Newton method in terms of an iteration over a sequence of linear systems:

$$\begin{aligned} \mathbf{J}(\mathbf{u}_k)\delta\mathbf{u} &= -\mathbf{R}(\mathbf{u}_n), \\ \mathbf{u}_{k+1} &= \mathbf{u}_k + s\delta\mathbf{u}, \\ k &= 0, 1, \dots \end{aligned} \quad (8)$$

where $\mathbf{J} \equiv \mathbf{R}' \equiv \partial\mathbf{R}/\partial\mathbf{u}$ is the Jacobian matrix. Starting the Newton procedure requires the specification of \mathbf{u}_0 . The scalar $s > 0$ can be chosen to improve convergence, for example, using a line search or under-relaxation/damping procedure, and is equal to unity in the classic Newton-Raphson approach. Iterations are performed over this system until the residual $\mathbf{R}(\mathbf{u}_n)$ and solution correction $\delta\mathbf{u}$ are sufficiently small, with appropriate normalisation.

For problems with N scalar equations and N scalar unknowns, the residual \mathbf{R} and solution \mathbf{u} vectors have dimensions of $N \times 1$. The components of the $N \times N$ Jacobian are

$$J_{ij} = \frac{\partial R_i(\mathbf{u})}{\partial u_j} \quad (9)$$

In the current work, we are interested in vector problems, where the governing momentum equation is formulated in terms of the unknown displacement solution vector. In this case, Equation 9 refers to the individual scalar components of the residual, solution, and Jacobian. That is, for 3-D analyses, the residual takes the form

$$\mathbf{R}(\mathbf{u}) = \{R_1^x, R_1^y, R_1^z, R_2^x, R_2^y, R_2^z, \dots, R_n^z\} \quad (10)$$

and the solution takes the form

$$\mathbf{u} = \{u_1^x, u_1^y, u_1^z, u_2^x, u_2^y, u_2^z, \dots, u_n^z\} \quad (11)$$

In practice, it is often more practical and efficient to form and store the residual, solution and Jacobian in a *blocked* manner, where the residual and solution can be considered as vectors of vectors. Similarly, the Jacobian can be formed in terms of sub-matrix block coefficients.

In the strict Newton procedure, the residuals converge at a quadratic rate when the current solution is close to the true solution; that is, the iteration error decreases proportionally to the square of the error at the previous iteration. Once the method gets sufficiently close to the true solution, the number of correct digits in the approximation roughly doubles with each iteration. However, quadratic convergence is only possible when using the exact Jacobian. In contrast, a quasi-Newton method uses an approximation to the Jacobian, sacrificing strict quadratic convergence in

an attempt to produce an overall more computationally efficient procedure. From this perspective, the segregated solution algorithm commonly employed in finite volume solid mechanics can be viewed as a quasi-Newton method, where an approximate Jacobian replaces the exact Jacobian:

$$\tilde{\mathbf{J}}(\mathbf{u}_k) \delta\mathbf{u} = -\mathbf{R}(\mathbf{u}_k) \quad (12)$$

In this case, the approximate Jacobian $\tilde{\mathbf{J}}$ comes from the compact stencil discretisation of a simple diffusion (Laplacian) term. A benefit of this approach is that the inter-component coupling is removed from the Jacobian, allowing the solution of three smaller scalar systems rather than one larger vector system in 3-D (or two smaller systems in 2-D).

A fully explicit procedure can also be viewed from this perspective by selecting a *diagonal* approximate Jacobian $\tilde{\mathbf{D}}$, making the solution of the linear system trivial:

$$\tilde{\mathbf{D}}(\mathbf{u}_k) \delta\mathbf{u} = -\mathbf{R}(\mathbf{u}_k) \quad (13)$$

2.3 Cell-Centred Finite Volume Discretisation

In this work, a nominally second-order cell-centred finite volume discretisation is employed. The solution domain is discretised in both space and time. The total simulation period is divided into a finite number of time increments, denoted as Δt , and the discretised governing momentum equation is solved iteratively in a time-marching fashion. The spatial domain is partitioned into a finite set \mathcal{P} of contiguous convex polyhedral cells, where each cell is denoted by $P \in \mathcal{P}$. A representative cell P is shown in Figure 1. The set of all faces of cell P is denoted by \mathcal{F}_P . This set is further subdivided into two disjoint subsets:

- **Internal Faces** ($\mathcal{F}_P^{\text{int}}$): Faces that are shared with neighbouring cells.
- **Boundary Faces** ($\mathcal{F}_P^{\text{bnd}}$): Faces that lie on the boundary of the spatial domain.

Each internal face $f_i \in \mathcal{F}_P^{\text{int}}$ corresponds to a neighbouring cell $N_{f_i} \in \mathcal{N}_P$, where \mathcal{N}_P is the set of all neighbouring cells of P . The outward unit normal vector associated with an internal face f_i is denoted by \mathbf{n}_{f_i} . The vector \mathbf{d}_{f_i} connects the centroid of cell P with the centroid of the neighbouring cell N_{f_i} .

The conservation equation (Equations 2, 3, or 4) is applied to each cell P and discretised in terms of the displacement at the centroid of the cell \mathbf{u}_P and the displacements $\mathbf{u}_{N_{f_i}}$ at the centroids of the neighbouring cells. Proceeding with the discretisation, the volume integrals and surface integrals in the governing equation are approximated by algebraic equations as described below.

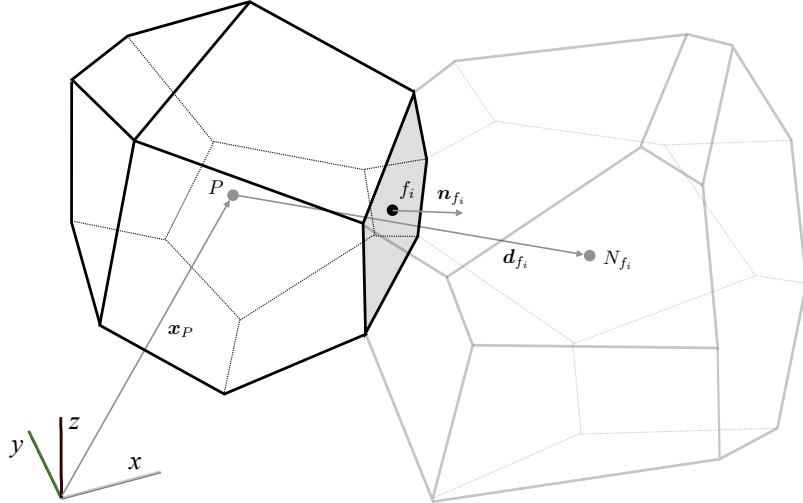


Fig. 1 Representative convex polyhedral cell P and neighbouring cell N_{f_i} , which share a face f_i

2.3.1 Volume Integrals

To discretise the volume integrals, the integrand ϕ is assumed to locally vary according to a truncated Taylor series expansion about the centroid of cell P :

$$\phi(\mathbf{x}) \approx \phi_P + (\mathbf{x} - \mathbf{x}_P) \cdot \nabla \phi_P \quad (14)$$

where subscript P indicates a value at the centroid of the cell P . Consequently, volume integrals over a cell P can be approximated to second order accuracy as

$$\begin{aligned} \int_{\Omega_P} \phi d\Omega_P &\approx \int_{\Omega_P} [\phi_P + (\mathbf{x} - \mathbf{x}_P) \cdot \nabla \phi_P] d\Omega_P \\ &\approx \phi_P \Omega_P \end{aligned} \quad (15)$$

where Ω_P is the volume of cell P and $\int_{\Omega_P} (\mathbf{x} - \mathbf{x}_P) d\Omega_P \equiv 0$ by definition of the cell centroid. This approximation corresponds to the midpoint rule and one point quadrature.

Using Equation 15, the inertia term (e.g. left-hand side term of Equation 2) becomes

$$\int_{\Omega_P} \rho \frac{\partial \mathbf{u}}{\partial t} d\Omega_P \approx \rho_P \left(\frac{\partial^2 \mathbf{u}}{\partial t^2} \right)_P \Omega_P \quad (16)$$

Similarly, the body force term (e.g. the second term on the right-hand side of Equation 2) becomes:

$$\int_{\Omega_P} \rho \mathbf{g} d\Omega_P \approx \rho_P \mathbf{g} \Omega_P \quad (17)$$

The discretisation of the acceleration in Equation 16 can be achieved using one of many finite difference schemes, e.g. first-order Euler, second-order backwards, second-order Newmark-beta. In

in the current work, the second-order backwards (BDF2) scheme is used:

$$\begin{aligned} \left(\frac{\partial^2 \mathbf{u}_P}{\partial t^2} \right)_P &\approx \frac{3\mathbf{v}_P^{[t+1]} - 4\mathbf{v}_P^{[t]} + \mathbf{v}_P^{[t-1]}}{2\Delta t} \\ &\approx \frac{3 \left(\frac{3\mathbf{u}_P^{[t+1]} - 4\mathbf{u}_P^{[t]} + \mathbf{u}_P^{[t-1]}}{2\Delta t} \right) - 4\mathbf{v}_P^{[t]} + \mathbf{v}_P^{[t-1]}}{2\Delta t} \end{aligned} \quad (18)$$

where Δt is the time increment – assumed constant here – and $\mathbf{v} = \partial \mathbf{u} / \partial t$ is the velocity vector. Superscript $[t]$ indicates the time level, with $\mathbf{u}_P^{[t+1]}$ corresponding to the unknown displacement at the current time step. Consequently, the displacement and velocity at the two previous time steps must be stored, or alternatively the displacement at the previous four time steps.

2.3.2 Surface Integrals

The surface integrals are discretised in a similar fashion to the volume integrals, where the integrand ϕ is assumed to locally vary according to a truncated Taylor series expansion about a face centroid \mathbf{x}_{f_i} :

$$\phi(\mathbf{x}) \approx \phi_f + (\mathbf{x} - \mathbf{x}_{f_i}) \cdot \nabla \phi_f \quad (19)$$

where subscript f indicates a value at the centroid of the face. Consequently, surface integrals about a cell P can be approximated to second order accuracy as

$$\begin{aligned} \oint_{\Gamma_P} \phi \, d\Gamma_P &= \sum_{f_i \in \mathcal{F}_P} \int_{\Gamma_{f_i}} \phi \, d\Gamma_{f_i} \\ &\approx \sum_{f_i \in \mathcal{F}_P} \int_{\Gamma_{f_i}} [\phi_{f_i} + (\mathbf{x} - \mathbf{x}_{f_i}) \cdot \nabla \phi_{f_i}] \, d\Gamma_{f_i} \\ &\approx \phi_{f_i} |\mathbf{\Gamma}_{f_i}| \end{aligned} \quad (20)$$

where Γ_P indicates the surface of cell P , subscript f_i indicates a quantity at the centroid of face f_i , and $\mathbf{\Gamma}_{f_i}$ indicates the area vector of face f_i .

Consequently, the surface integral term (e.g. first term on the right-hand side of Equation 2), corresponding to the divergence of stress, can be discretised as

$$\oint_{\Gamma_P} \mathbf{n} \cdot \boldsymbol{\sigma} \, d\Gamma_P \approx \sum_{f_i \in \mathcal{F}_P} \mathbf{\Gamma}_{f_i} \cdot \boldsymbol{\sigma}_{f_i} \quad (21)$$

The stress $\boldsymbol{\sigma}_{f_i}$ at a face is calculated by linear interpolation from the adjacent cell centres [36]:

$$\boldsymbol{\sigma}_{f_i} = w_{f_i} \boldsymbol{\sigma}_P + (1 - w_{f_i}) \boldsymbol{\sigma}_{N_{f_i}} \quad (22)$$

where the interpolation ratio is defined as $w_{f_i} = (\mathbf{n}_{f_i} \cdot [\mathbf{x}_{N_{f_i}} - \mathbf{x}_{f_i}]) / (\mathbf{n}_{f_i} \cdot [\mathbf{x}_{N_{f_i}} - \mathbf{x}_P])$.

The cell-centred stress is calculated as a function of the displacement gradient according to the chosen mechanical law, where the cell-centre displacement gradients are determined using a first-neighbours least squares method [36]:

$$(\nabla \mathbf{u})_P = \sum_{f_i \in \mathcal{F}_P} \omega_{f_i}^2 \mathbf{G}_{f_i}^{-1} \cdot \mathbf{d}_{f_i} (\mathbf{u}_{N_{f_i}} - \mathbf{u}_P) \quad (23)$$

where the least squares weight is $\omega_{f_i} = 1/|\mathbf{d}_{f_i}|$. The \mathbf{G}_{f_i} tensor is

$$\mathbf{G}_{f_i} = \sum_{f_i \in \mathcal{F}_P} \omega_{f_i}^2 \mathbf{d}_{f_i} \mathbf{d}_{f_i} \quad (24)$$

The $\mathbf{G}_{f_i}^{-1} \cdot \mathbf{d}_{f_i}$ vectors are purely a function of the mesh and can be computed once and stored.

Update above to allow for boundary contributions

2.3.3 Rhie-Chow Stabilisation

To quell zero-energy solution modes (i.e. checkerboarding oscillations), a Rhie-Chow-type stabilisation term [34] is added to the residual (Equation 5). The Rhie-Chow stabilisation term $\mathcal{D}_{\text{Rhie-Chow}}$ for a cell P takes the following form:

$$\mathcal{D}_{\text{Rhie-Chow}} = \sum_{f \in N_f} \alpha \bar{K}_f \left[|\Delta_f| \frac{\mathbf{u}_{N_f} - \mathbf{u}_P}{|\mathbf{d}_f|} - \Delta_f \cdot (\nabla \mathbf{u})_f \right] |\Gamma_f| \quad (25)$$

where $\alpha > 0$ is a user-defined parameter for globally scaling the amount of stabilisation. Parameter \bar{K}_f is a stiffness-type parameter that gives the stabilisation an appropriate scale and dimension. Here, $\bar{K}_f = \frac{4}{3}\mu + \kappa = 2\mu + \lambda$ following previous work [8, 10, 35], where μ is the shear modulus (first Lamé parameter), κ is the bulk modulus, and λ is the second Lamé parameter. The vector $\Delta_f = \mathbf{d}_f / \mathbf{d}_f \cdot \mathbf{n}_f$ is termed the *over-relaxed orthogonal* vector [36]. The face gradient $(\nabla \mathbf{u})_f$ is calculated by interpolation from adjacent cell centres. In Equation 25, the first term within the brackets on the right-hand side represents a compact stencil (two-node) approximation of the face normal gradient, while the second term represents a larger stencil approximation. These two terms cancel out in the limit of mesh refinement (or if the solution varies linearly); otherwise, they produce a stabilisation effect that tends to smooth the solution fields. As the term reduces at a third-order rate, it does not affect the overall scheme's second-order accuracy.

2.3.4 Boundary Conditions

Enforcing boundary conditions involves modifying the discretised surface integrals at the boundaries faces. Three types of boundary condition are considered here: prescribed displacement, prescribed traction, and symmetry planes.

Include: When calculating cell-centre gradients in cells adjacent to the boundary, known boundary values are used for displacement boundaries, whereas traction boundary faces are excluded.

Two terms must be approximated on a boundary face b :

$$\int_{\Gamma_b} K_{imp} \mathbf{n}_b \cdot [\nabla (\Delta \mathbf{u})]_b d\Gamma_b \quad (26)$$

which comes from Equation 36, and

$$\int_{\Gamma_b} (j_b \mathbf{f}_b^{-T} \cdot \mathbf{n}_b) \cdot \boldsymbol{\sigma}_b d\Gamma_b \quad (27)$$

which comes from Equation ??, where subscript b indicates a quantity at a boundary face in the updated configuration.

Equation 26 must be discretised both implicitly and explicitly (deferred correction), as per Equation ??, while Equation 27 is discretised explicitly. The Rhie-Chow term is set to zero on boundary faces, and all geometric terms (\mathbf{n}_b , Γ_b) are calculated on the updated configuration.

Five classes of boundary conditions are employed in the current work (prescribed displacement, prescribed traction, symmetry plane, axisymmetric/wedge, frictional contact) as described below. An additional boundary condition where the normal component of the displacement is prescribed and the shear traction is zero is also used; the discretisation of this condition employs the prescribed displacement condition in the boundary normal direction and the traction condition in the tangential direction.

Prescribed displacement

The displacement boundary condition, a Dirichlet condition, may be constant in time or time-varying and fixes the value of \mathbf{u} at the centre of a boundary face. The corresponding displacement increment at the boundary face $\Delta \mathbf{u}_b = \mathbf{u}_b^{[m+1]} - \mathbf{u}_b^m$ is substituted into the calculation of the surface normal gradient term in Equation 26. The resulting contribution of a boundary face b to the discretised Laplacian term becomes:

$$\begin{aligned} \int_{\Gamma_b} K_{imp} \mathbf{n}_b \cdot [\nabla (\Delta \mathbf{u})]_b d\Gamma_b &\approx K_{imp}^b |\Delta_b| \left(\frac{\Delta \mathbf{u}_b - \Delta \mathbf{u}_P}{|\mathbf{d}_b|} \right) |\Gamma_b| \\ &+ K_{imp}^b \mathbf{k}_b \cdot [\nabla (\Delta \mathbf{u})]_P |\Gamma_b| \end{aligned} \quad (28)$$

where \mathbf{d}_b connects the cell centre \mathbf{C}_P with the boundary face centre \mathbf{C}_b in the updated configuration, and the non-orthogonal correction vector $\mathbf{k}_b = (\mathbf{I} - \mathbf{n}_b \mathbf{n}_b) \cdot \mathbf{d}_b$.

Prescribed traction

The traction boundary condition, constant in time or time-varying, is implemented by replacing $\mathbf{n}_f \cdot \boldsymbol{\sigma}_f$ on boundary faces with the known prescribed traction \mathbf{t}_b . Following calculation of the cell-centred displacements, displacements on traction boundary faces \mathbf{u}_b is calculated by extrapolation

from the adjacent cell centre:

$$\mathbf{u}_b = \mathbf{u}_P + (\mathbf{x}_b - \mathbf{x}_P) \cdot (\nabla \mathbf{u})_P \quad (29)$$

where subscript b indicates a value at the centre of a boundary face, and P indicates a value at the centre of the adjacent cell.

Symmetry plane

On a symmetry plane normal component of displacement is zero, and the tangential gradient of displacement is zero. For boundary faces on a symmetry plane, the mirror reflection $(\Delta \mathbf{u})_N$ of the cell-centre displacement increment $(\Delta \mathbf{u})_P$ can be obtained as

$$\begin{aligned} (\Delta \mathbf{u})_N &= \mathbf{R}_m \cdot (\Delta \mathbf{u})_P \\ &= (\mathbf{I} - 2\mathbf{n}_b \mathbf{n}_b) \cdot (\Delta \mathbf{u})_P \end{aligned} \quad (30)$$

where \mathbf{R}_m is termed the reflection tensor. The discretisation in Equation 36 takes the same form, but the neighbour cell-centre values are replaced by the mirror reflected values for boundary faces on the symmetry plane. The \mathbf{d}_b vector at a symmetry plane boundary face is calculated as

$$\mathbf{d}_b = \mathbf{R}_m \cdot \mathbf{C}_P - \mathbf{C}_P \quad (31)$$

This means that symmetry planes are orthogonal by definition, and the non-orthogonal correction (second term on the right-hand side of Equation 36) drops out.

In the current work, the cell-centre values are corrected for skewness errors, resulting in the following contribution to the Laplacian term at a symmetry boundary face (Equation 28):

$$\int_{\Gamma_{u_b}} K_{imp} \mathbf{n}_b \cdot \nabla (\Delta \mathbf{u}) d\Gamma_b = K_{imp}^b |\Delta_b| \left(\frac{\Delta \mathbf{u}_N^* - \Delta \mathbf{u}_P^*}{|\mathbf{d}_b|} \right) |\Gamma_b| \quad (32)$$

where the skew-corrected cell-centre values are

$$\Delta \mathbf{u}_P^* = \Delta \mathbf{u}_P + [(\mathbf{I} - \mathbf{n}_b \mathbf{n}_b) \cdot \mathbf{d}_b] \cdot [\nabla (\Delta \mathbf{u})]_P \quad (33)$$

$$\Delta \mathbf{u}_N^* = \mathbf{R}_m \cdot (\Delta \mathbf{u})_P^* \quad (34)$$

Displacement increment values on the symmetry planes are calculated as

$$(\Delta \mathbf{u})_b = \frac{(\Delta \mathbf{u})_P^* + (\Delta \mathbf{u})_N^*}{2} \quad (35)$$

Further details on the implementation of symmetry planes in segregated cell-centred finite volume formulations can be found in [?].

3 Solution Algorithms

3.1 Segregated Solution Algorithm

The classic segregated solution algorithm can be viewed as a quasi-Newton method, where a compact-stencil approximation of a diffusion term is employed as the approximate Jacobian:

$$\begin{aligned}\tilde{\mathbf{J}} &= \oint_{\Gamma} \bar{K} \mathbf{n} \cdot \nabla \mathbf{u} d\Gamma \\ &\approx \sum_{f \in N_f} \bar{K}_f |\Delta_f| \left(\frac{\mathbf{u}_{N_f} - \mathbf{u}_P}{|\mathbf{d}_f|} \right) |\Gamma_f|\end{aligned}\quad (36)$$

When a diffusion term is typically discretised using the cell-centre finite volume method, non-orthogonal corrections are included in a deferred correction manner to preserve the order of accuracy on distorted grids. However, in the current quasi-Newton method form, the approximate Jacobian's exact value does not affect the final converged solution, but only the convergence behaviour. Consequently, non-orthogonal corrections are not included in the approximate Jacobian here. However, grid distortion is appropriately accounted for in the calculation of the residual. Nonetheless, as a result, it is expected that the convergence behaviour of the segregated approach may degrade as mesh non-orthogonality increases.

The linearised system (Equation 12) is formed for each cell in the domain, resulting in a system of algebraic equations:

$$[\tilde{\mathbf{J}}] [\delta \mathbf{u}] = -[\mathbf{R}(\mathbf{u}_n)] \quad (37)$$

where $[\tilde{\mathbf{J}}]$ is a symmetric, weakly diagonally dominant, $M \times M$ stiffness matrix, where M is three times the number of cells in 3-D and twice the number of cells in 2-D. By design, matrix $[\tilde{\mathbf{J}}]$ contains no inter-component coupling; consequently, three equivalent smaller linear systems can be formed and solved for the Cartesian components of the displacement correction (or two in 2-D), e.g.

$$[\tilde{\mathbf{J}}_x] [\Delta \mathbf{u}_x] = -[\mathcal{R}_x(\mathbf{u}_n)] \quad (38)$$

$$[\tilde{\mathbf{J}}_y] [\Delta \mathbf{u}_y] = -[\mathcal{R}_y(\mathbf{u}_n)] \quad (39)$$

$$[\tilde{\mathbf{J}}_z] [\Delta \mathbf{u}_z] = -[\mathcal{R}_z(\mathbf{u}_n)] \quad (40)$$

where \bullet_x represents the components in the x direction, \bullet_y represents the components in the y direction, and \bullet_z represents the components in the z direction. An additional benefit of the segregated approach, from a memory perspective, is that matrices $[\tilde{\mathbf{J}}_x]$, $[\tilde{\mathbf{J}}_y]$ and $[\tilde{\mathbf{J}}_z]$ are identical, except for the effects from including boundary conditions. From an implementation perspective, this allows a single scalar matrix to be formed and stored, where the boundary condition contributions are inserted before solving a particular component.

The *inner* linear sparse systems (Equations 38, 39 and 40) can be solved using any typical direct or iterative linear solver approach; however, an incomplete Cholesky pre-conditioned conjugate

gradient method [37] is often preferred as the weakly diagonally dominant characteristic leads to good convergence characteristics. Algebraic multigrid can be used to accelerate convergence.

In literature, the segregated solution algorithm is typically formulated in terms of the total displacement vector (or its difference between time steps) as the primary unknown; in contrast, in the quasi-Newton interpretation presented here, the primary unknown is the correction to the displacement vector, which goes to zero at convergence. Nonetheless, both approaches are equivalent and neither formulation displays superior performance.

3.2 Jacobian-free Newton-Krylov Algorithm

As noted in the introduction, the Jacobian-free Newton-Krylov avoids the need to construct the Jacobian matrix explicitly by approximating its action on a solution vector using the finite difference method, repeated here:

$$\mathbf{J}\mathbf{v} \approx \frac{\mathbf{F}(\mathbf{x} + \epsilon\mathbf{v}) - \mathbf{F}(\mathbf{x})}{\epsilon} \quad (41)$$

The derivation of this approximation can be shown for a 2×2 system as [20]:

$$\begin{aligned} \frac{\mathbf{F}(\mathbf{x} + \epsilon\mathbf{v}) - \mathbf{F}(\mathbf{x})}{\epsilon} &= \left(\begin{array}{c} \frac{F_1(x_1 + \epsilon v_1, x_2 + \epsilon v_2) - F_1(x_1, x_2)}{\epsilon} \\ \frac{F_2(x_1 + \epsilon v_1, x_2 + \epsilon v_2) - F_2(x_1, x_2)}{\epsilon} \end{array} \right) \\ &\approx \left(\begin{array}{c} \frac{F_1(x_1, x_2) + \epsilon v_1 \frac{\partial F_1}{\partial u_1} + \epsilon v_2 \frac{\partial F_1}{\partial u_2} - F_1(x_1, x_2)}{\epsilon} \\ \frac{F_2(x_1, x_2) + \epsilon v_1 \frac{\partial F_2}{\partial u_1} + \epsilon v_2 \frac{\partial F_2}{\partial u_2} - F_2(x_1, x_2)}{\epsilon} \end{array} \right) \\ &\approx \left(\begin{array}{c} v_1 \frac{\partial F_1}{\partial u_1} + v_2 \frac{\partial F_1}{\partial u_2} \\ v_1 \frac{\partial F_2}{\partial u_1} + v_2 \frac{\partial F_2}{\partial u_2} \end{array} \right) \\ &\approx \mathbf{J}\mathbf{v} \end{aligned} \quad (42)$$

where a first-order truncated Taylor series expansion about \mathbf{u} was used to approximate $\mathbf{F}(\mathbf{x} + \epsilon\mathbf{v})$. As noted above, choosing an appropriate value for ϵ is non-trivial, and care must be taken to balance truncation error (reduced by decreasing ϵ) and round-off error (increased by decreasing ϵ).

The purpose of preconditioning the Jacobian-free Newton-Krylov method is to reduce the number of inner linear solver iterations. In the current work, the GMRES linear solver is used for the inner system. Using right preconditioning, the finite difference approximation of Equation 41 becomes

$$\mathbf{J}\mathbf{P}^{-1}\mathbf{v} \approx \frac{\mathbf{F}(\mathbf{x} + \epsilon\mathbf{P}^{-1}\mathbf{v}) - \mathbf{F}(\mathbf{x})}{\epsilon} \quad (43)$$

where \mathbf{P} is the preconditioning matrix or process. In practice, only the action of \mathbf{P}^{-1} on a vector is required, and the \mathbf{P}^{-1} may not be explicitly formed. Concretely, the preconditioner needs to approximately solve the linear system $\mathbf{y} = \mathbf{P}^{-1}\mathbf{v}$.

In the current work, we propose to use the compact-stencil approximate Jacobian from the segregated algorithm $\tilde{\mathbf{J}}$ as the preconditioning matrix \mathbf{P} for the preconditioned Jacobian-free Newton-Krylov method. This preconditioning approach can be considered as a “physics-based” preconditioner in the classifications of Knoll and Keyes [20]. The approach is conceptually similar to an approximation of the Jacobian of a higher-order advection scheme by a compact-stencil lower-order upwind scheme. A benefit of the proposed approach is that existing segregated frameworks can re-use their existing discretisation and storage implementations. Concretely, the Jacobian-free Newton-Krylov method requires only a procedure for forming this preconditioning matrix and a procedure for explicitly evaluating the residual. Both routines are easily implemented – and are likely already available – in an existing segregated framework. The only additional required procedure is an interface to an existing Jacobian-free Newton-Krylov implementation. In the current work, the PETSc package [31] is used as the nonlinear solver, driven by a finite volume solver in the OpenFOAM toolbox [33] (OpenFOAM-v2312).

Several preconditioners are available in the literature, incomplete Cholesky or ILU(k) being popular; however, multigrid methods offer the greatest potential for large-scale problems. As noted by Knoll and Keyes [20], algorithmic simplifications within a multigrid procedure, which may result in loss of convergence for multigrid as a solver, have a much weaker effect when multigrid is the preconditioner. In this work, three preconditioners are considered:

1. ILU(k): incomplete LU with fill-in k.
2. Multigrid: the HYPRE Boomerang [38] multigrid implementation.
3. LU: the MUMPS [39, 40] direct solver.

A challenge with Newton-type methods, including Jacobian-free versions, is poor convergence when far from the true solution, and divergence is often a real possibility. Globalisation refers to steering an initial solution towards the quadratic convergence range of the Newton method. Several strategies are possible, and it is common to combine approaches [20]. In the current work, a line search procedure is used to select the s parameter in the solution update step (the second line in Equations 8). Line search methods assume the Newton update direction is correction and aim to find a scalar $s > 0$ that decreases the residual $\mathbf{R}(\mathbf{u}_k + s\delta\mathbf{u}) < \mathbf{R}(\mathbf{u}_k)$. The scalar s is typically ≤ 1 , but extrapolation (> 1) is also possible for accelerating convergence, albeit at the expense of robustness. In addition to a line search approach, a *transient continuation* globalisation approach is used in the current work, where a prediction for the solution (displacement) field at time $t + \Delta t$ is performed at the start of a new time step, based on a truncated second-order Taylor series expansion:

$$\mathbf{u}_{t+\Delta t} = \mathbf{u}_t + \Delta t \left(\frac{\partial \mathbf{u}}{\partial t} \right)_t + \frac{1}{2} \Delta t^2 \left(\frac{\partial^2 \mathbf{u}}{\partial t^2} \right)_t \quad (44)$$

where \mathbf{v}_t is the velocity at time t , and $\left(\frac{\partial \mathbf{v}}{\partial t} \right)_t$ is the acceleration at time t . In this way, for highly nonlinear problems, the user can decrease the time step size Δt as a globalisation approach to improve the performance of the Newton method. The predictor step in Equation 44 has been chosen to be consistent with the assumed discretisation of the temporal term in the governing equation; that is, the second order backwards scheme.

A final comment on the Jacobian-free Newton-Krylov solution algorithm is the potential importance of *oversolving*. Here, oversolving refers to solving the linear system to too tight a tolerance during the early Newton iterations, essentially wasting time when the solution is far from the true solution. In addition, some authors [20] have shown Newton convergence to be worse when the earlier iterations are solved to too tight a tolerance. The concept of oversolving also applies to segregated solution procedures and has been well-known since the early work of Demirdžić and co-workers [7], where the residuals are typically reduced by one order of magnitude in the inner linear system. In the current work, the residual is reduced by one order of magnitude in the segregated approach and three orders in the Jacobian-free Newton-Krylov approach.

4 Test Cases

This section compares the performance of the proposed Jacobian-free Newton-Krylov solution approach with the segregated approach on several benchmark cases. The cases have been chosen to exhibit a variety of characteristics in terms of

- Geometric dimension (2-D vs. 3-D),
- Geometric nonlinearity (small strain vs. large strain),
- Geometric complexity (basic geometric shapes vs. complex geometry),
- Statics vs. dynamics, and
- Material behaviour (elasticity, elastoplasticity, hyperelasticity).

In all cases, the residuals are dropped by six orders of magnitude unless stated otherwise.

The presented analyses aim to be extensive but not exhaustive; several common features of modern solid mechanics procedures are left for future work, including contact mechanics and incompressibility.

The remainder of this section is structured as follows: The proposed discretisation's accuracy and order are assessed on several test cases of varying dimensions and phenomena. Subsequently, the remaining sub-sections assess the efficiency of the Jacobian-free Newton-Krylov approach compared with the standard segregated procedure.

4.1 Testing the Accuracy and Order of Accuracy

This section solely focuses on assessing the accuracy and order of accuracy of the discretisation. Assessment of the computational efficiency regarding time and memory requirements is left to the subsequent sections.

Case 1: Order Verification via the Manufactured Solution Procedure

The first test case consists of a $0.2 \times 0.2 \times 0.2$ m cube with linear elastic ($E = 200$ GPa, $\nu = 0.3$) properties. A manufactured solution for displacement (Figure 2(a)) is employed of the form:

$$\mathbf{u} = \begin{pmatrix} a_x \sin(4\pi x) \sin(2\pi y) \sin(\pi z) \\ a_y \sin(4\pi x) \sin(2\pi y) \sin(\pi z) \\ a_z \sin(4\pi x) \sin(2\pi y) \sin(\pi z) \end{pmatrix} \quad (45)$$

where $a_x = 2 \times 10^{-6}$ m, $a_y = 4 \times 10^{-6}$ m, and $a_z = 6 \times 10^{-6}$ m. The Cartesian coordinates are given by x , y and z . The corresponding manufactured body force term is given in Appendix B.

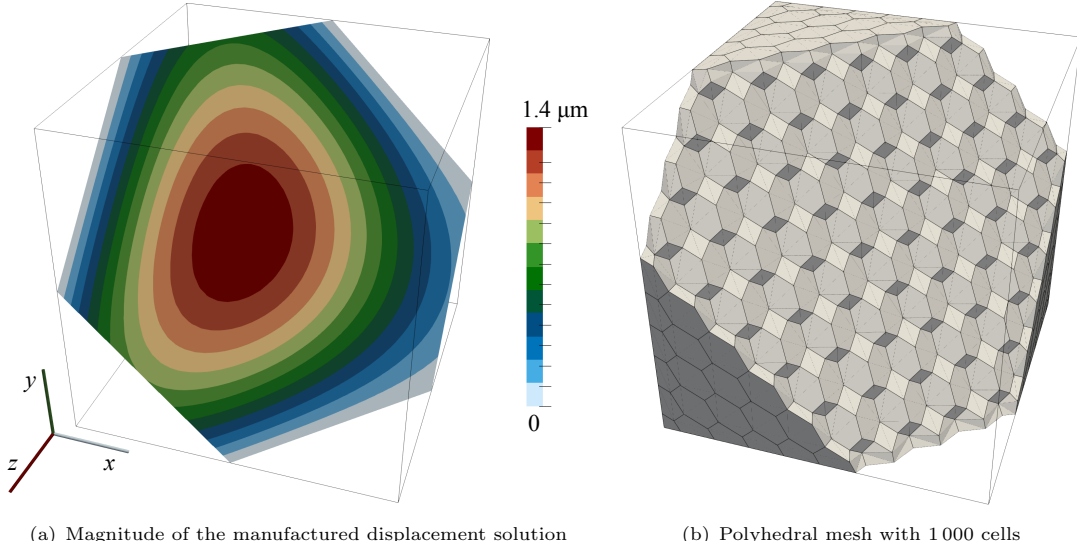


Fig. 2 A cut plane through the cube case geometry showing the magnitude of the manufactured displacement solution (left) and a polyhedral mesh (right). The cut plane passes through the centre of the cube and has the unit normal $\mathbf{n} = (1/\sqrt{3} \quad 1/\sqrt{3} \quad 1/\sqrt{3})$.

The manufactured displacement solution is applied at the domain's boundaries, and inertial effects are neglected. Three mesh types are examined: (i) hexahedra, (ii) tetrahedra, and (iii) regular polyhedra (Figure 2(b)). The hexahedral meshes are created using the OpenFOAM `blockMesh` utility, while the tetrahedral meshes are created using Gmsh [41]. To create the polyhedral meshes, the tetrahedra meshes are converted to their dual polyhedral representations using the OpenFOAM `polyDualMesh` utility. Starting from an initial mesh spacing of 0.04 m, six meshes are created by successively halving the spacing. The cell numbers for the hexahedral and polyhedral meshes are 125, 1 000, 8 000, 64 000, 512 000, and 4 096 000, while the tetrahedral mesh cell counts are 384, 4 374, 41 154, 355 914, 2 958 234, and 24 118 074. For the same average cell width, the cell counts show that the tetrahedral meshes have larger cell counts by a factor of 3 to 6.

Figure 3(a) shows the displacement magnitude discretisation errors (L_2 and L_∞) as a function of the average cell width for all three mesh types (hexahedral, tetrahedral and polyhedral), while Figure 3(b) shows the corresponding order of accuracy plots. For ease of interpretation, the symbol shapes in the figures have been chosen to correspond to the cell shapes: a square for hexahedra,

a triangle for tetrahedra and a pentagon for polyhedra. The maximum (L_∞) and average (L_2) discretisation errors are seen to reduce at an approximately second-order rate for all mesh types, except for the L_2 error on the hexahedral meshes, which is approximately 2.3 on the finest grid.

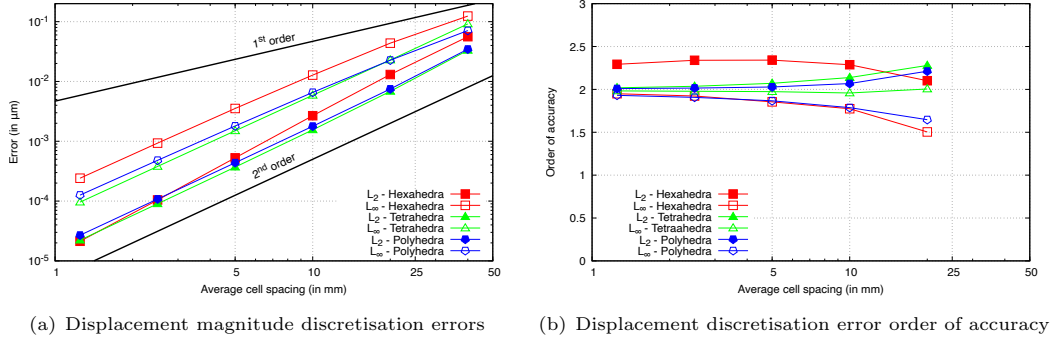


Fig. 3 Manufactured solution cube case: the accuracy and order of accuracy for displacement magnitude

The predicted σ_{xx} stress distribution for a hexahedral mesh with 512 000 cells is shown in Figure 4(a). The corresponding cell-wise σ_{xx} error distribution is shown in Figure 4(b). The errors of greatest magnitude (43 kPa) occur at the boundaries, corresponding to where the local truncation error is higher due to the use of one-sided differencing. The discretisation errors in the stress

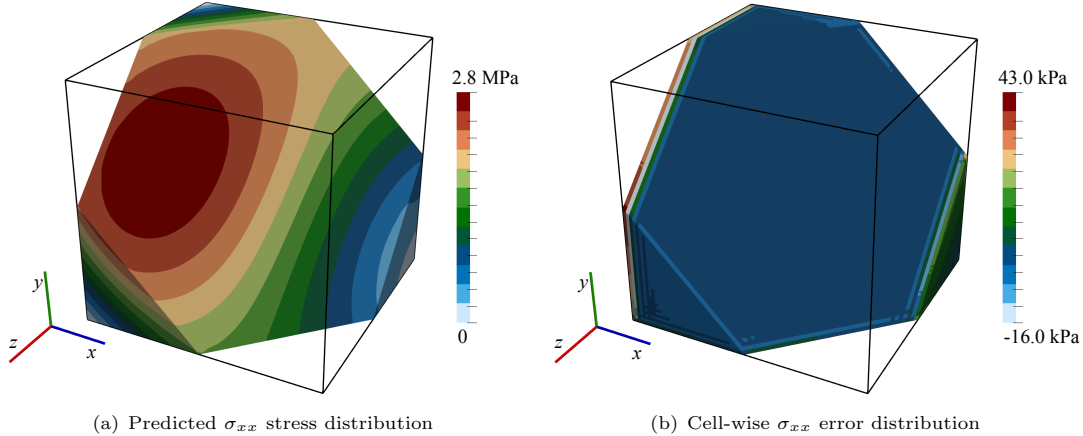


Fig. 4 Manufactured solution cube case: the predicted σ_{xx} stress distribution on a cut-plane for the hexahedral mesh with 512 000 cells (left).

magnitude are shown in Figure 5(a), and the order of accuracy in Figure 5(b). The order of accuracy for the average (L_2) stress error is seen to be approximately 1.5 for the hexahedral and polyhedral meshes. In contrast, the average stress error order for the tetrahedral meshes is 1. Similarly, the maximum (L_∞) stress order of accuracy is seen to approach 1 for all three mesh types.

The presented results have been generated using the Jacobian-free Newton-Raphson solution algorithm; however, minimal differences were seen when using the segregated solution algorithm, and hence, the segregated results are not shown.

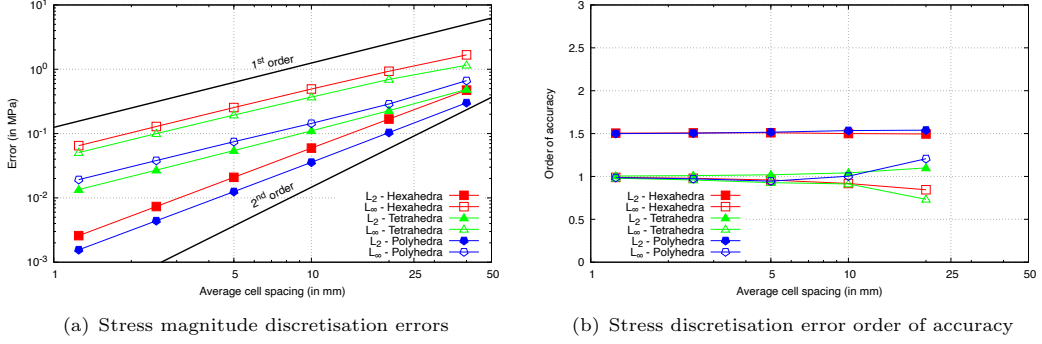


Fig. 5 Manufactured solution cube case: the accuracy and order of accuracy for stress magnitude

Case 1b: Spherical Cavity in an Infinite Solid Subjected to Remote Stress

This 3-D problem consists of a spherical cavity with radius $a = 0.2$ m (Figure 6) in an infinite, isotropic linear elastic solid ($E = 200$ GPa, $\nu = 0.3$). Far from the cavity, the solid is subjected to a tensile stress $\sigma_{zz} = T = 1$ MPa, with all other stress components zero. The analytical expressions

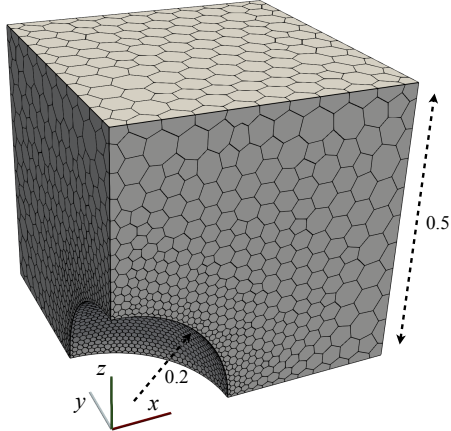


Fig. 6 Spherical cavity case geometry, showing the polyhedral mesh with 4539

for the stress and displacement distributions are given in Appendix C.

The computational solution domain is taken as one-eighth of a $1 \times 1 \times 1$ m cube aligned with the Cartesian axes, with one corner at the centre of the sphere. The analytical tractions are applied at the far boundaries of the domain to mitigate the effects of finite geometry. Unstructured polyhedral meshes are employed with grading towards the cavity. The cell sizes at the cavity surfaces are 100, 50, 25, 12.5, 6.25, and 3.125 mm, and the corresponding cell counts are 976, 4552 (Figure 6), 29 611, 213 100, 614 261. Initially, unstructured tetrahedral meshes were generated using the Gmsh meshing utility [41], followed by conversion to their dual polyhedral representations using the OpenFOAM `polyDualMesh` utility.

The spherical cavity case errors seem to approach zero order accuracy. Maybe we have hit the precision limit...? We may leave this case out

Case 2: Out-of-plane bending of an elliptic plate

This 3-D, static, linear elastic test case (Figure 7) consists of a thick elliptic plate (0.6 m thick) with a centred elliptic hole, with the inner and outer ellipses given as

$$\left(\frac{x}{2}\right)^2 + \left(\frac{y}{1}\right)^2 = 1 \text{ inner ellipse} \quad (46)$$

$$\left(\frac{x}{3.25}\right)^2 + \left(\frac{y}{2.75}\right)^2 = 1 \text{ outer ellipse} \quad (47)$$

The case has been described by the National Agency for Finite Element Methods and Standards (NAFEMS) [42], and analysed using finite volume procedures by Demirdžić et al. [43] and Cardiff et al. [44]. Symmetry allows one-quarter of the geometry to be simulated. A constant pressure of 1 MPa is applied to the upper surface, and the outer surface is fully clamped. The mechanical properties are: $E = 210$ GPa, $\nu = 0.3$. Six successively refined hexahedral meshes are used, with cell counts of 45, 472 (Figure 7), 4140, 34968, 287280 and 2438242.

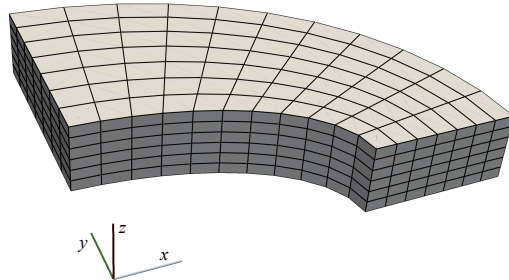


Fig. 7 Elliptic Plate geometry and mesh containing 472 hexahedral cells

The predictions for the equivalent (von Mises) stress along the line $r = \sqrt{x^2 + y^2} = 2.1$ m, $z = 0.3$ m is shown in Figure 8. The results from the finest grid in Demirdžić et al. [43] are given for comparison, where good agreement is seen; the small offset between the finest mesh predictions and those from Demirdžić et al. [43] are likely due to errors introduced when extracting the Demirdžić et al. [43] results using WebPlotDigitizer [45]. The sample values have been calculated by generating 40 uniformly spaced angles between 0 and $\frac{\pi}{2}$ along the line, finding the cell of each sampled point, and extrapolating from the cell-centred value using the field gradient.

Case 3: Narrow T-section component under tension

This case, proposed by Demirdžić et al. [43], consists of a narrow engineering component with a T cross-section (Figure 9). The case is 3-D, static, with linear elastic material behaviour. Symmetry allows one-quarter of the geometry to be simulated. A constant negative pressure of 1 MPa is applied to the lower surface, and the upper left surface is fully clamped. The Young's modulus is $E = 210$ GPa, and Poisson's ratio is $\nu = 0.3$. A radius 5 mm hole is located at the expected stress concentration.

Five successively refined hexahedral meshes are created using the OpenFOAM `blockMesh` utility, consisting of 624, 4992, 39936, 319488, and 2555904 cells. The corresponding average cell

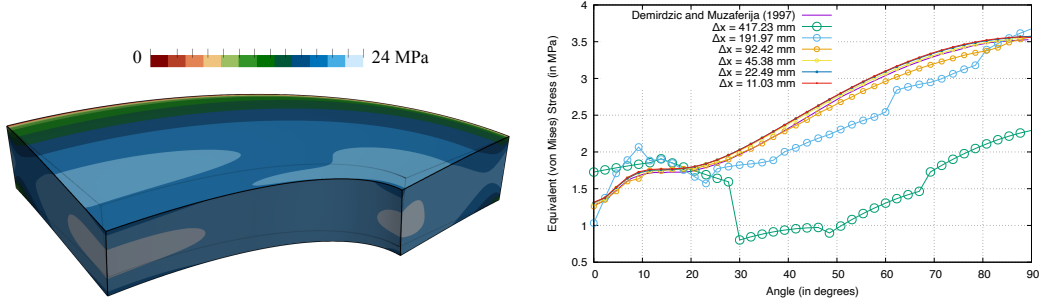


Fig. 8 Equivalent (von Mises) stress distribution in the elliptic plate

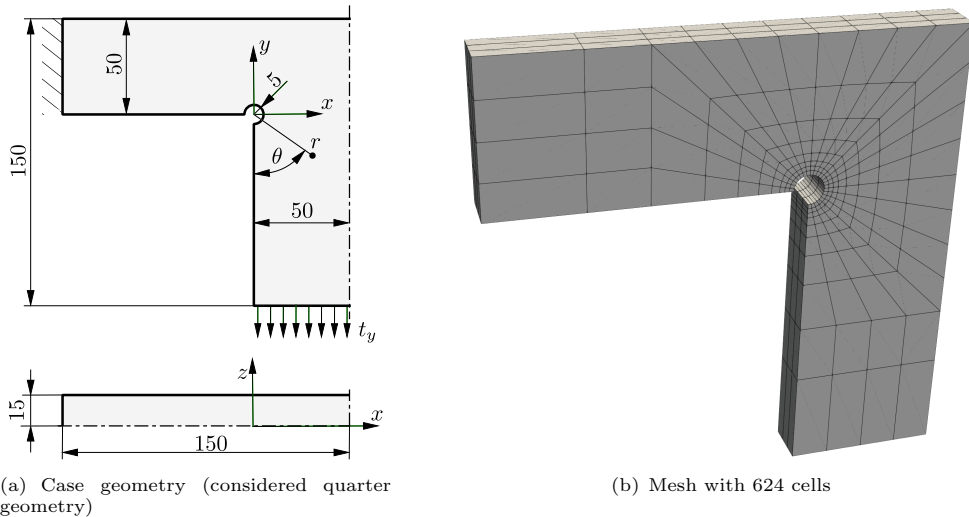


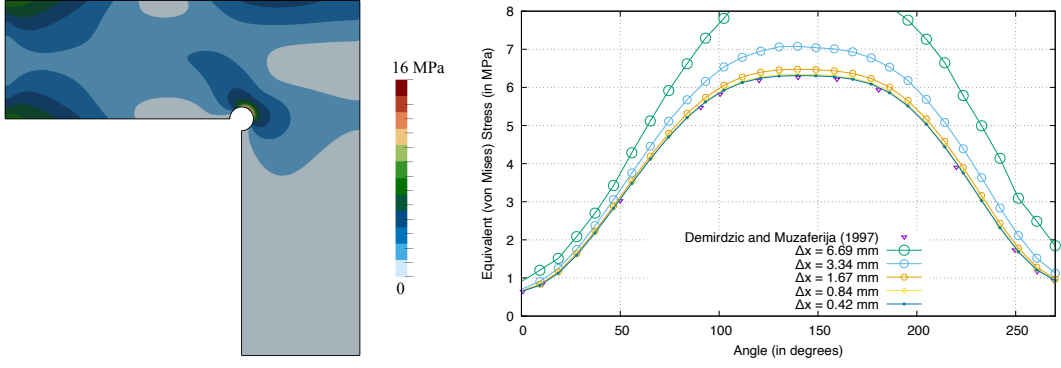
Fig. 9 Narrow T-section component under tension: geometry and mesh

widths—calculated as the cubed root of the total domain volume divided by the number of cells—are 6.69, 3.34, 1.67, 0.84, and 0.42 mm.

The predicted equivalent (von Mises) stress distribution on the $z = 0$ plane is shown in Figure 10(a), where a stress concentration is apparent near the hole. The equivalent stress along the line $r = 1.5R$, $z = 0$ is shown for the different meshes in Figure 10(b), where R is the hole radius. The predictions are seen converge to the results reported in Demirdžić et al. [43]. Similarly to the elliptic plate case, the sample values have been to by generating 30 uniformly spaced angles between $-\frac{\pi}{2}$ and $-\pi$ along the line, finding the cell of each sampled point, and extrapolating from the cell-centred value using the field gradient.

Case 4: Inflation of an idealised ventricle

Inflation of an idealised ventricle (Figure 11) was proposed by Land et al. [46] as a benchmark problem for cardiac mechanics software. The case is 3-D, static, with finite hyperelastic strains.



(a) Equivalent stress distribution for the mesh with 2 555 904 cells on the $z = 0$ m plane

(b) Equivalent stress along the line $r = 1.5R$, $z = 0$ m

Fig. 10 Equivalent (von Mises) stress distribution in the narrow T-section component under tension

The initial geometry is defined as a truncated ellipsoid:

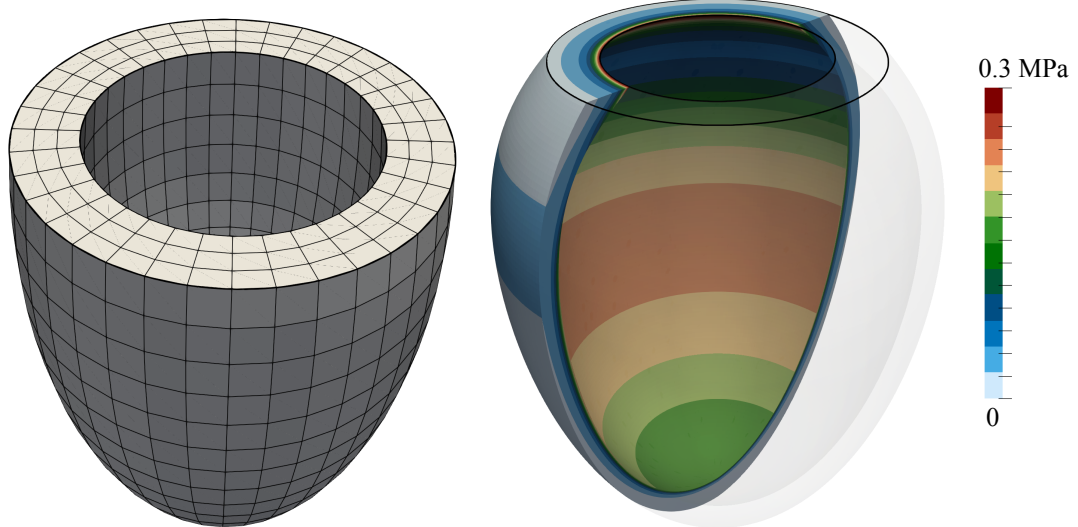
$$x = r_s \sin(u) \cos(v), \quad y = r_s \sin(u) \sin(v), \quad z = r_l \cos(u) \quad (48)$$

where on the inner (endocardial) surface $r_s = 7$ mm, $r_l = 17$ mm, $u \in [-\pi, -\arccos(\frac{5}{17})]$ and $v \in [-\pi, \pi]$, while on the outer (epicardial) surface $r_s = 10$ mm, $r_l = 20$ mm, $u \in [-\pi, -\arccos(\frac{5}{20})]$ and $v \in [-\pi, \pi]$. The base plane $z = 5$ mm is implicitly defined by the ranges for u . The hyperelastic material behaviour is described by the transversely isotropic constitutive proposed by Guccione et al. [47] law, where the parameters are $C = 10$ kPa, $b_f = b_t = b_{fs} = 1$. The benchmark specifies an incompressible material; in the current work, incompressibility is enforced weakly using a penalty approach, where the bulk modulus parameter is chosen to be two orders of magnitude greater ($\kappa = 1000$ kPa) than the greatest shear modulus parameter. The chosen parameters produce isotropic behaviour. A pressure of 10 kPa is applied to the inner surface, and the base plane is fixed. The geometry is meshed using a structured approach and is predominantly composed of hexahedra, with prism cells forming the apex. The OpenFOAM utilities `blockMesh` and `extrudeMesh` are used to create the meshes. Four successively refined meshes are examined: 1 620 (shown in Figure 11(a)), 12 960, 103 680, and 829 440 cells. The case can be simulated as 2-D axisymmetric but is simulated here using the full 3-D geometry.

The equivalent (von Mises) stress at full inflation is shown for the mesh with 829,440 cells in Figure 11(b), where the high stresses on the endocardial (inner) surface quickly drop off through the wall thickness towards the epicardial (outer) surface. The predicted deformed configuration of the midline of the ventricle wall is shown in Figure 12, where a side-by-side comparison is given with the round-robin benchmark results from Land et al. [46]. The predictions are seen to become quickly mesh-independent and fall within the benchmark ranges.

Case 5: Cook's membrane

Cook's membrane (Figure 13) is a well-known bending-dominated benchmark case used in linear and non-linear analysis. The 2-D plane strain tapered panel (trapezoid) is fixed on one side and subjected to uniform shear traction on the opposite side. The vertices of the trapezoid (in mm) are



(a) Ventricle undeformed geometry, showing the mesh with 1,620 cells
(b) Cross-section showing the equivalent (von Mises) stress distribution for the mesh with 829,440 cells

Fig. 11 Idealised ventricle case

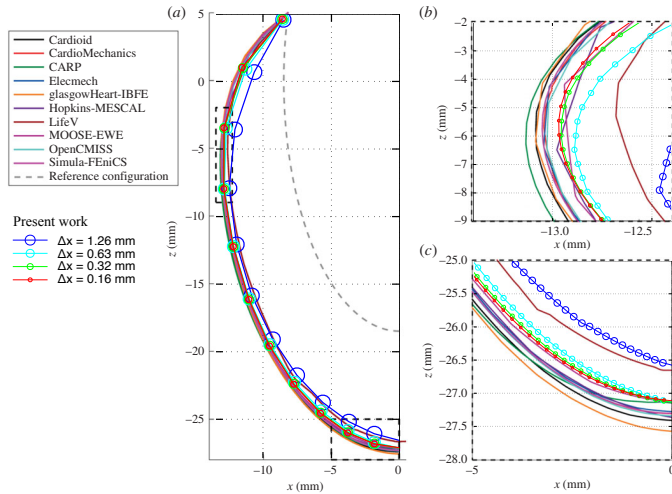


Fig. 12 Idealised ventricle: predictions for the four meshes from the present work overlaid on the round-robin predictions from Land et al. [46]

$(0, 0)$, $(48, 44)$, $(48, 60)$, and $(0, 44)$. The problem is solved quasi-statically, using 30 equally-sized loading increments, and there are no body forces.

The current work considers three forms of the problem:

- Small strain linear elastic [48, 49]: $E = 70$ MPa, $\nu = 1/3$, and $\tau = 6250$ Pa.
- Finite strain neo-Hookean hyperelastic [50]: $E = 1.0985$ MPa, $\nu = 0.3$, and $\tau = 0.0625$ MPa.
- Finite strain elastoplastic [49, 51, 52]: $E = 206.9$ MPa, $\nu = 0.29$, $\sigma_y = 0.45 + 0.12924\bar{\varepsilon}_p + (0.715 - 0.45)(1 - e^{-16.93\bar{\varepsilon}_p})$ MPa, and $\tau = 0.3125$ MPa.

where E is the Young's modulus, ν is the Poisson's ratio, σ_y is the yield strength, $\bar{\varepsilon}_p$ is the equivalent plastic strain, and τ is the prescribed shear traction. Seven successively refined quadrilateral meshes are considered, where the cell counts are 9, 36, 144 (Figure 13(b)), 576, 2 304, 9 216, and 36 864.

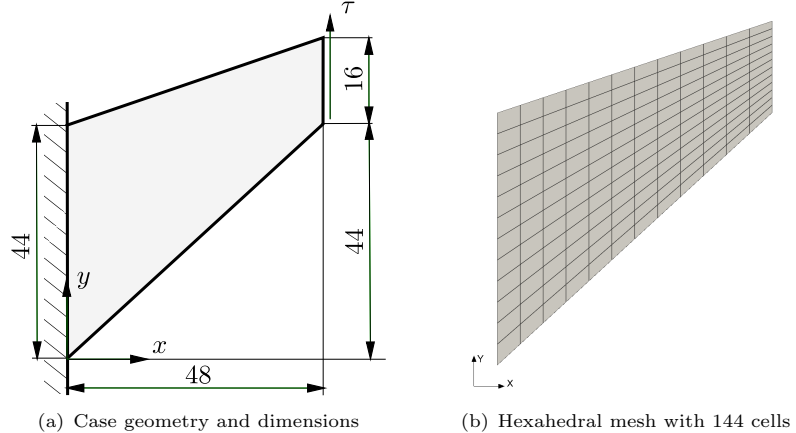


Fig. 13 Cook's membrane case geometry and mesh

Figure 14 shows the predicted equivalent stress distribution on the mesh with 36 842 cells for linear elastic, hyperelastic and hyperelastoplastic cases. The stress distribution is consistent with bending, with regions of high stress near the upper and lower surfaces and a line of relatively unstressed material in the centre. The greatest equivalent stresses occur at the top-left corner and the lower surface. In the hyperelastoplastic case, almost the entire domain is plastically yielding with only a small thin region remaining elastic, indicated by the blue line in Figure 14(c).

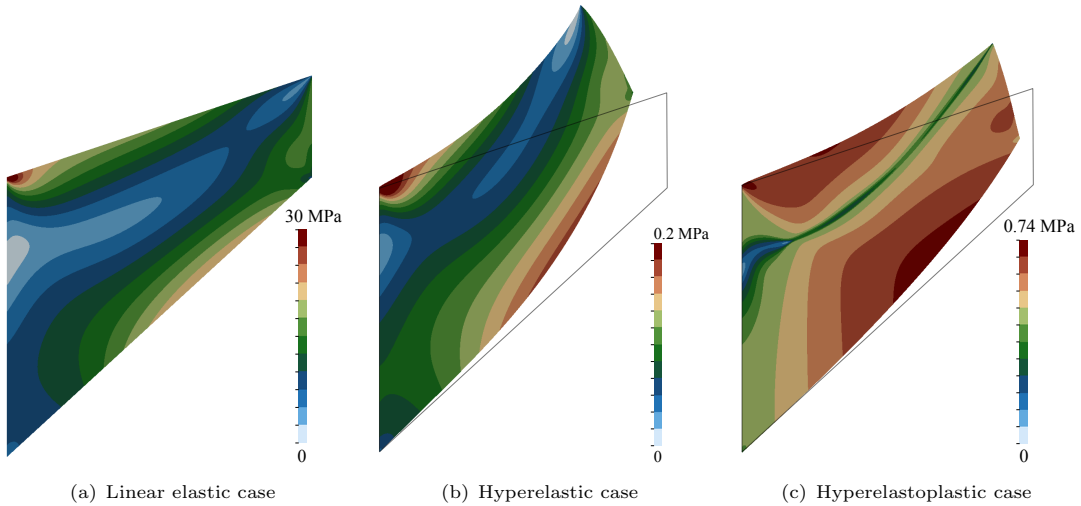


Fig. 14 Equivalent (von Mises) stress distribution for the three Cook's membrane cases using the mesh with 36 842 cells

Figure 15 compares the predicted vertical displacement at the reference point as a function of the average cell widths with results from the literature. The reference point is taken as the top right point – (48,60) mm – in the elastic and hyperelastoplastic cases, while it is taken as the midway point of the loading surface – (48,52) mm – in the hyperelastic case.

No difference is seen in the predictions whether using the Jacobian-free Newton-Krylov or segregated approach, assuming convergence is achieved. This is expected since both use the same discretisation, and the solution tolerances are shown to ensure the iteration errors are small. Consequently, only the Jacobian-free Newton-Krylov results are shown for the linear elastic and

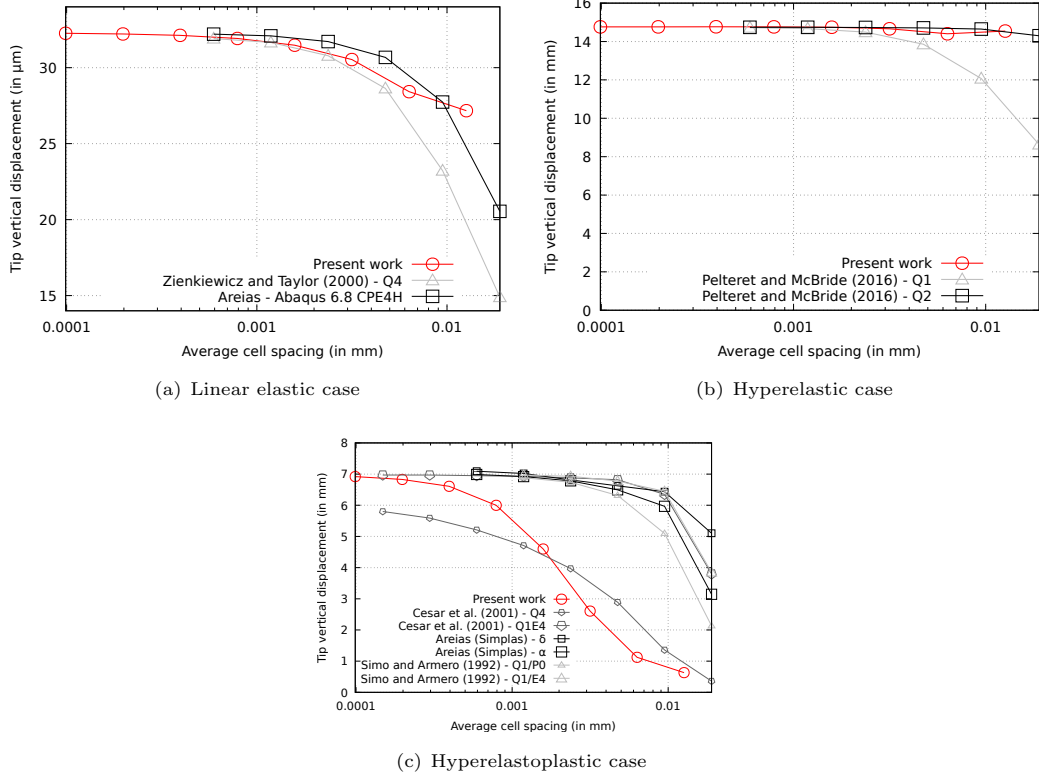


Fig. 15 Cook's membrane vertical displacement predictions at the reference point as a function of the average cell width. Comparisons are given with the results from [48–51].

hyperelastic cases. However, the Jacobian-free Newton-Krylov showed poor convergence in the hyperelastoplastic case and failed to converge on many of the meshes. As a result, the results for the segregated approach are presented instead for the hyperelastoplastic case. Discussion of the relative convergence and robustness of the Jacobian-free Newton-Krylov and segregated methods is left to Section 4.2.

Case 6: Vibration of a 3-D Cantilevered Beam

This 3-D, dynamic, finite strain case geometry consists of a $2 \times 0.2 \times 0.2$ m cuboid column and was proposed in its initial form by Tuković and Jasak [53]. A sudden, constant traction $\mathbf{T} = (0.1, 0.1, 0)$ MPa is applied to the upper surface. A neo-Hookean hyperelastic material is assumed with $E = 15.293$ MPa, $\nu = 0.3$ and density $\rho = 1000 \text{ kg m}^{-3}$, while the area $A = 0.04 \text{ m}^2$ and the second moment of area $I = \frac{1}{7500} \text{ m}^4$. The geometric and material parameters were chosen for the first natural frequency to be 1 Hz in the small strain limit. The magnitude of the applied traction was chosen to ensure significant geometric nonlinearity, with the upper surface of the beam expected to drop below the plane of the lower surface. Four successively refined hexahedral meshes are generated using the OpenFOAM `blockMesh` utility, with cell counts of 270, 2160, 17280 and 138240. The time step size is 1 ms, and the total period is 10 s.

The deformed configuration of the beam at six time steps is shown in Figure 16(a) for the mesh with 2160 cells, where the upper surface is seen to drop below the horizontal from approximately

$t = 0.2$ s to 0.32 s. The corresponding displacement magnitude of the centre of the upper surface of the beam vs time is shown in Figure 16(b).

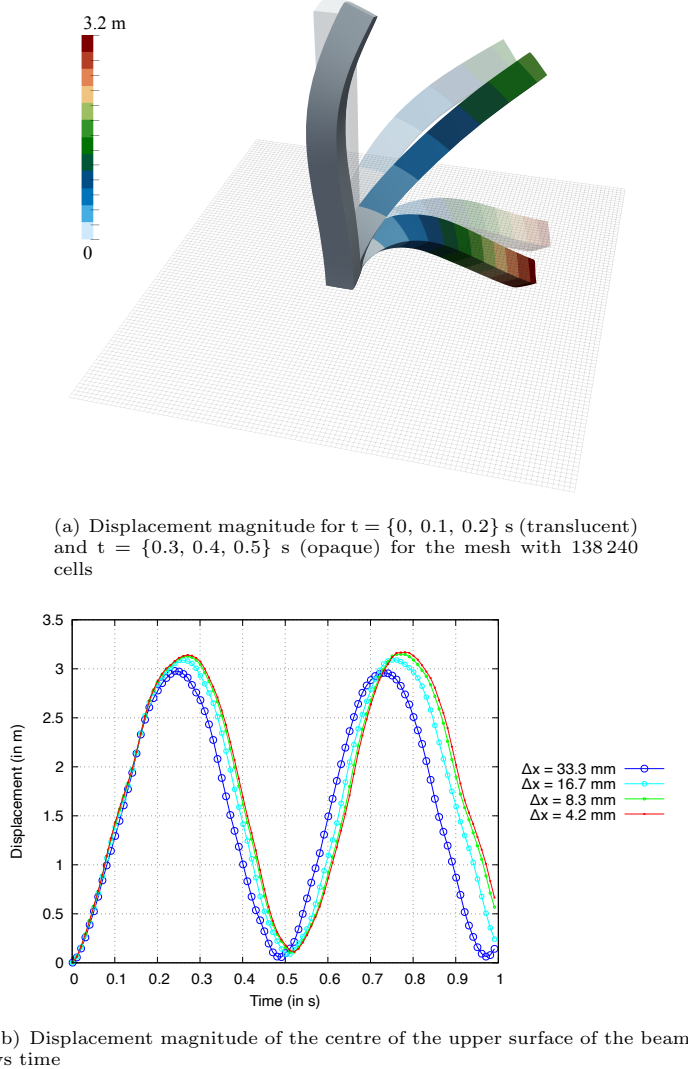


Fig. 16 Deflection of a 3-D Cantilevered Beam

Case 7: Axial Turbine Blade

This 3-D, quasi-static, small strain, linear elastic case consists of a twisted axial turbine blade (Figure 17) with the Cartesian axis-aligned bounding box $105.55 \times 177.628 \times 336.5$ mm. This case demonstrates the application of the proposed approach to an industrially-relevant geometry. The blade is constrained at the rotation axis end and subjected to a centrifugal body force $\mathbf{f}_b = \rho\omega^2\mathbf{r}$ kg m $^{-2}$ s $^{-2}$. The scalar rotational velocity $\omega = \frac{2\pi\text{RPM}}{60}$ is defined here about the x axis, where RPM = 720. The vector \mathbf{r} is defined as the shortest vector to the rotation (x) axis. The blade's root is constrained, while all other surfaces are traction-free. A linear elastic material is assumed with $E = 4.431$ GPa, $\nu = 0.33$, and $\rho = 1200$ kg m $^{-3}$. An unstructured polyhedral mesh with 322 161 cells is employed (Figure 17), created in Ansys Fluent and converted to the OpenFOAM format using the `fluent3DMeshToFoam` OpenFOAM utility. Could we include a finer mesh?

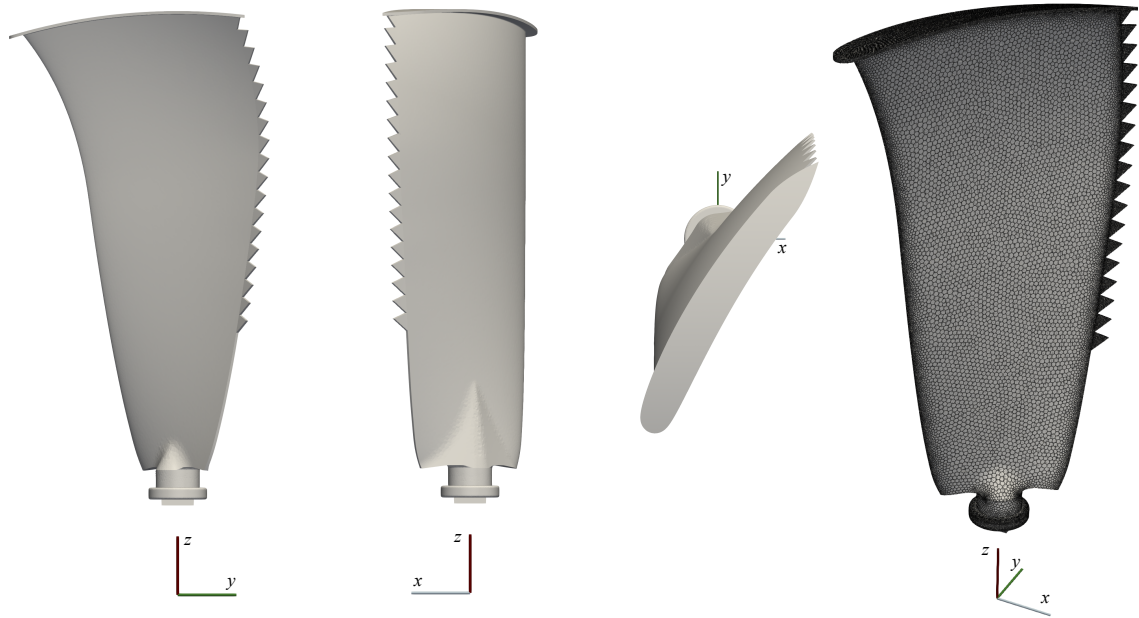


Fig. 17 Axial turbine blade case geometry

The prediction displacement magnitude distribution (left image in Figure 18) is consistent with a cantilever with the largest deflection occurring at the distal free-end of the turbine. The equivalent (von Mises) stress distribution (right image in Figure 18) shows the peak stresses to occur near the blade root and leading and trailing edges, with concentrations near the trailing edge vortex generators **correct name?**.

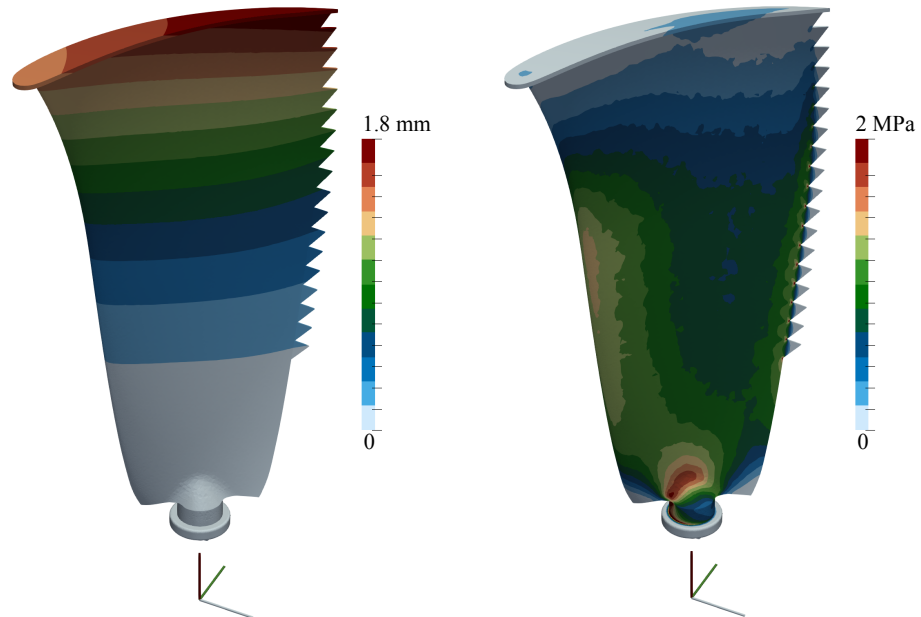
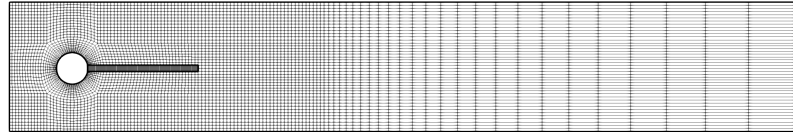


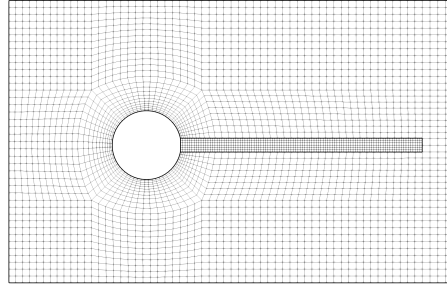
Fig. 18 Axial turbine blade displacement magnitude and equivalent stress distributions **non-smooth stress contours =** indicative of low order of accuracy

Case 8: Elastic plate behind a rigid cylinder

Turek and Hron [54] proposed this well-known fluid-solid interaction benchmark case as an extension of the classic flow around a cylinder in a channel problem [55]. The FSI3 variant of the case examined here (Figure 19) consists of a horizontal channel (0.41 m in height, 2.5 m in length) with a rigid cylinder of radius 0.05 m, where the cylinder centre is 0.2 m from the bottom and inlet (left) boundaries. A parabolic velocity is prescribed at the inlet velocity with a mean value of 2 m/s. A St. Venant-Kirchhoff hyperelastic plate ($E = 5.6 \text{ MPa}$, $\nu = 0.4$) of 0.35 m in length and 0.02 m in height is attached to the right-hand side of the rigid cylinder. The fluid model is assumed to be isothermal, incompressible, and laminar and adopts the segregated PIMPLE solution algorithm. The fluid's kinematic viscosity is $0.001 \text{ m}^2/\text{s}$ and density is 1000 kg/m^3 , while the solid's density is $10\,000 \text{ kg/m}^3$. The interface- quasi-Newton with inverse Jacobian from a least-squares model coupling approach [56] is employed for the fluid-solid interaction coupling. The fluid-solid interface residual is reduced by four orders of magnitude within each time step. Further details of the fluid-solid interaction procedure are found in Tuković et al. [57]. Three successively refined quadrilateral meshes are employed: The fluid region meshes have 1 252, 5 008, and 20 032 cells, while the solid region meshes have 156, 624 and 2 496 cells. The total simulation time is 20 s, and the time-step size is 0.5 ms.



(a) Mesh containing 5 336 cells in the fluid region and 630 cells in the solid region, where a closeup of the plate is shown in the right



(b) Close-up of the mesh around the plate

Fig. 19 Elastic plate behind a rigid cylinder case geometry and mesh

Figure 20 shows the velocity field in the fluid region and displacement magnitude in the solid region at $t = 4.42 \text{ s}$, corresponding to a peak in the vertical displacement of the plate free-end oscillation. The fluid is seen to accelerate as it passes the cylinder, with regular vortices being thrown off the plate, causing it to oscillate. The predicted mean, amplitude and frequency of the vertical and horizontal displacement of the end of the plate are compared with the results from Turek and Hron [54] in Table 1. As directed in Turek and Hron [54], the maximum and minimum

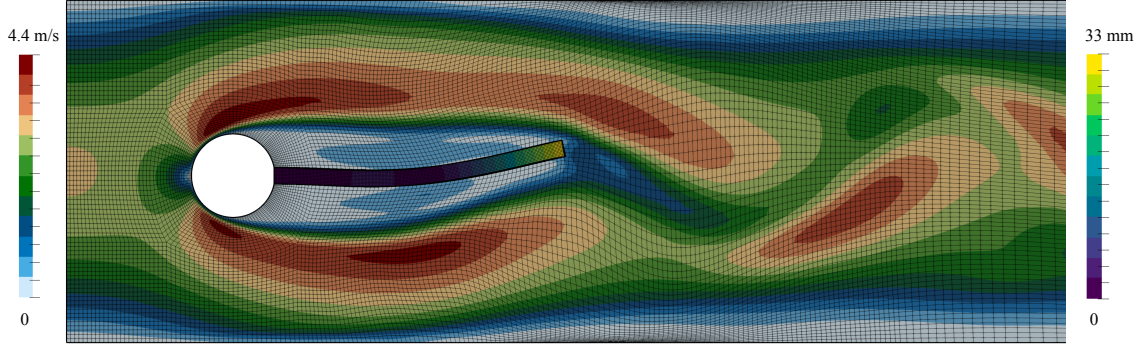


Fig. 20 Elastic plate behind a rigid cylinder case results at $t = 20$ s for the mesh with 20 032 cells in the fluid region and 2 496 in the solid region. The velocity magnitude is shown in the fluid region while the displacement magnitude is shown in the solid region.

values for the last period are used to calculate the mean and amplitude:

$$\text{mean} = \frac{1}{2}(\max + \min), \quad \text{amplitude} = \frac{1}{2}(\max - \min) \quad (49)$$

while the frequency is calculated as the inverse of the period.

Mesh (number of fluid and solid cells)	u_x (in mm)	u_y (in mm)
1 (1 252 + 156)	-0.1 ± 0.001 [47.6]	1.58 ± 0.002 [5.88]
2 (5 008 + 624)	-2.16 ± 2.00 [10.2]	1.54 ± 29.56 [5.6]
3 (20 032 + 2 496)	-2.51 ± 2.37 [12.1]	0.87 ± 33.08 [5.6]
Turek and Hron [54]	-2.69 ± 2.53 [10.9]	1.48 ± 34.38 [5.3]

Table 1 Average predicted displacements (mean \pm amplitude [frequency]) of the free end of the plate. Note that large-scale plate oscillations in mesh 1 (coarsest mesh) die out within the first 10 s.

4.2 Resource Requirements and Robustness

This section compares resource requirements and robustness of the Jacobian-free Newton-Krylov and segregated approaches on the cases presented in Section 4.1. Specifically, time and memory requirements are analysed, and cases where either approach diverges are examined. In some cases, time and memory requirements from finite element software **Abaqus** are given for reference. In all cases, the Jacobian-free Newton-Krylov approach used the generalised minimal residual method (GMRES) linear solver with the direct LU preconditioner for 2-D and the Hypre *BoomerAMG* multigrid preconditioner for 3-D. In contrast, The segregated approach used the conjugate gradient linear solver and the Hypre *BoomerAMG* multigrid preconditioner for all cases. Time and memory requirements are implementation and hardware-specific; nonetheless, it is insightful to see the relative performances of the Jacobian-free Newton-Krylov and segregated approaches on the same hardware and within the same implementation framework. Clock times and memory usage (measured with the GNU time utility) were generated using a Mac Studio with an M2 Ultra CPU on one CPU core, where the code was built with the Clang compiler. Examination of multi-CPU-core parallelisation is left to Section 4.5.

Table 2 lists the wall clock times (time according to a clock on the wall) and maximum memory usage for all cases and all meshes. Figure 22(a) plots the corresponding speedup on all cases as a function of the number of degrees of freedom, where the speedup is defined as the segregated clock time divided by the Jacobian-free Newton-Krylov clock time. The number of degrees of freedom is $2\times$ the cell count in 2-D cases and $3\times$ in 3-D cases, except in the fluid-solid interaction case where the fluid domain has three degrees of freedom (two velocity components and pressure) in 2-D. Speedup is only calculated for clock times greater than 2 seconds to avoid the comparison of small numbers. In all cases where convergence was achieved, the Jacobian-free Newton-Krylov approach was faster (speedup > 1), with speedups of one or two orders of magnitude in many cases. Additionally, it can be observed from Figure 22(a) that the speedup increases as the number of degrees of freedom increases. The largest speedup was 237 on the finest mesh of the membrane i (2-D, linear elastic) case, while the lowest speed was 1.09 and occurred on the coarsest mesh in the fluid-solid interaction case. Excluding the fluid-solid interaction, where the majority of degrees of freedom are placed in the fluid region, the next lowest speed-up was 1.66 and occurred on a coarse mesh in the membrane ii (2-D, hyperelastic) case.

Figure 21(b) shows the *relative memory* usage, defined here as the maximum memory usage of the segregated approach divided by that of the Jacobian-free Newton-Krylov approach. The relative memory usage is close to unity in most cases, indicating there is no significant increase in memory requirements when switching from a segregated approach to a Jacobian-free Newton-Krylov approach. In addition, unlike for the speedup, there is no general trend in the relative memory usage as the number of degrees of freedom increases. The maximum value for relative memory was 1.9 and occurred in the second-finest mesh for the membrane ii (2-D, hyperelastic) case, although for all other meshes in this case, the value was less than one (between 0.82 and 0.95). The maximum memory usage is primarily attributed to the linear solver and preconditioner; the choice of preconditioner and linear solver settings are examined further in Section 4.3.

Note: we use segregated in PETSc, so it is a vector system

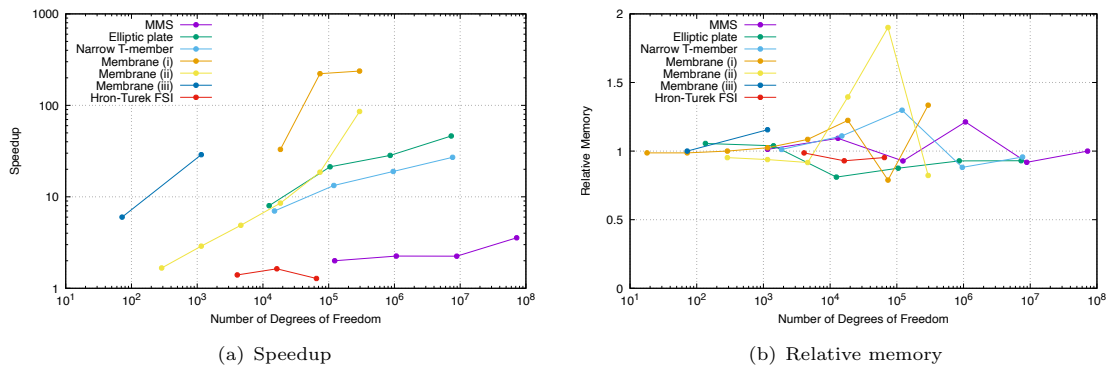


Fig. 21 The speedup (segregated clock time divided by the Jacobian-free Newton-Krylov clock time) and relative memory usage (segregated maximum memory usage divided by the Jacobian-free Newton-Krylov maximum memory usage) as a function of degrees of freedom

Regarding robustness, the Jacobian-free Newton-Krylov approach converged in all cases bar one, requiring less than five outer Newton iterations on average in all converged cases. The only case where the Jacobian-free Newton-Krylov approach failed to converge was for the Membrane iii

Case	Cell Count	JFNK		Segregated	
		Time (in s)	Memory (in MB)	Time (in s)	Memory (in MB)
MMS	384	0	78	0	79
<i>3-D, static, linear elastic</i>	4 374	0	86	0	94
	41 154	1	195	2	181
	355 914	4	1 063	9	1 289
	2 958 234	41	6 724	92	6 174
	24 118 074	486	30 606	1 732	30 601
Elliptic	45	0	72	0	76
Plate	472	0	78	0	81
<i>3-D, static, linear elastic</i>	4 140	1	153	8	124
	34 968	7	754	149	660
	287 280	95	3 943	2 694	3 661
	2 438 242	988	21 884	45 692	20 348
T-member	624	0	84	1	85
<i>3-D, static, linear elastic</i>	4 992	1	127	7	141
	39 936	10	557	133	723
	319 488	154	4 024	2 916	3 547
	2 555 904	1 751	22 814	47 344	21 827
Ventricle	1 620	54	133	†	†
<i>3-D, static, hyperelastic</i>	12 960	576	553	†	†
	103 680	8 362	3 435	†	†
	829 440	150 023	11 746	†	†
Membrane i	9	0	77	0	76
<i>2-D, static, linear elastic</i>	36	0	77	0	76
	144	0	78	0	78
	576	0	82	1	84
	2 304	0	94	4	102
	9 216	1	152	33	186
	36 864	2	497	444	392
	147 456	10	1 461	2 371	1 950
Membrane ii	9	1	81	1	78
<i>2-D, static, hyperelastic</i>	36	1	81	2	78
	144	3	84	5	80
	576	9	97	26	91
	2 304	34	144	166	132
	9 216	161	256	1 374	357
	36 864	860	554	15 991	1 053
	147 456	1 585	2 847	135 851	2 341
Membrane iii	9	0	78	3	78
<i>2-D, static, hyperelastoplastic</i>	36	1	79	6	79
	144	†	†	27	82
	576	8	90	231	104
	2 304	†	†	1 379	180
	9 216	†	†	8 321	451
	36 864	†	†	60 698	1 396
	147 456	†	†	341 212	3 466
Cantilever	270	11	85	†	†
<i>3-D, dynamic, hyperelastic</i>	2 160	71	181	†	†
	17 280	854	752	†	†
	138 240	11 800	5 790	†	†
Turbine	322 161	22 782	11 102	rnmg to-rn	
<i>3-D, static, linear elastic</i>	2 493 299	to-rn		rnmg to-rn	
FSI	1 252 + 156	3 830	748	5 360	738
<i>2-D, dynamic, hyperelastic</i>	5 008 + 624	32 074	834	52 372	775
	20 032 + 2 496	170 919	785	218 797	748

Table 2 Execution times (rounded to the nearest second) and maximum memory usage for Jacobian-free Newton-Krylov (JFNK) and segregated methods (rounded to the nearest MB). † indicates the solver crashed.

problem, the only elastoplastic case examined. For the failed meshes, they each reached approximately 80% of the total load before the linear solver diverged. The cause of this divergence is likely related to the proposed compact preconditioner matrix, which is formulated based on small *elastic* strains, being a poor approximation of the true Jacobian for large plastic strains. Interestingly, convergence problems were not encountered in the hyperelastic cases (Membrane ii, Ventricle,

Cantilever, Fluid-solid interaction), demonstrating that the proposed compact *linear elastic* preconditioner matrix is suitable for such large strain hyperelastic cases. In contrast, the segregated approach—which uses the same matrix—had no problems with the elastoplastic case (Membrane iii) but failed to converge on two of the hyperelastic cases (Ventricle, Cantilever). In both cases where the segregated approach failed, large elastic strains and large rotations were observed, and the segregated solver failed in the early time steps. It is interesting to note that the same linear elastic preconditioner matrix works well with the Jacobian-free Newton-Krylov approach for hyperelastic cases but not for the segregated approach, while the opposite is true for elastoplastic cases.

Regarding geometric dimension, the same general trends are observed in 2-D and 3-D, with no major distinctions in behaviour. The same can be said for geometric nonlinearity (small strain vs. large strain) with similar speed-ups for both linear elastic and hyperelastic cases. One observation worth highlighting is the relatively lower speed for the method of manufactured solutions case (3-D, linear elastic): a possible explanation is that the segregated approach has previously been seen to be efficient on geometry with low aspect ratios (ratio of maximum to minimum dimensions); in this case, the aspect ratio is at its minimum (unity). In contrast, in other 3-D, linear elastic cases (Elliptic plate, Narrow T-Member, Membrane i, Turbine), the aspect ratios are greater than unity, and the segregated approach performs worse relative to the Jacobian-free Newton-Krylov approach.

Should we add Table 1 for other hardware in the appendix?

4.3 Effect of the Preconditioner Choice

This section examines the effect of preconditioning procedure choice on the performance of the Jacobian-free Newton Krylov approach. Three choices of preconditioning procedure are compared:

- **LU** - The *Multifrontal Massively Parallel sparse direct Solver* (MUMPS) [39, 40] LU decomposition direct solver. A direct solver is expected to be the more robust but may suffer from excessive time and memory requirements for larger numbers of unknowns.
- **ILU(N)** - Incomplete LU decomposition with N fill-in. ILU(N) is expected to have lower memory requirements than the LU direct solver but at the expense of robustness. As the system of unknowns becomes larger, the number of ILU(N) iterations is expected to increase. As the fill-in factor N increases, ILU(N) approaches the behaviour of a LU direct solver.
- **Algebraic multigrid** - The Hypre Boomerang [38] parallelised multigrid preconditioner. Multigrid approaches have the potential to offer superior performance than other methods for larger problems, with near linear scaling of time and memory requirements.

An additional consideration when selecting a preconditioner is its ability to scale in parallel as the number of CPU cores increases. From this perspective, the iterative approaches (ILU(N) and multigrid) are expected to show better parallel scaling than direct methods (LU). Analysis of this point is left to Section 4.5.

The preconditioning approaches are compared in three cases: membrane i (2-D, linear elastic), elliptic plate (3-D, linear elastic), and idealised ventricle (3-D, hyperelastic).

Figure 22 compares the clock times and maximum memory requirements for the three preconditioning approaches as a function of degrees of freedom. ILU1 diverges on the ventricle for the finer two meshes: re-rnng with ILU2 LU ventricle: mesh4 is running Comment on the results: e.g. fastest, slowest, most/least iterations, etc Provide insights, if any: e.g. why is one faster or slower Conclusion: which preconditioner is 'best' for which situation: probably LU is best for 'small' cases and multigrid for 'large' cases

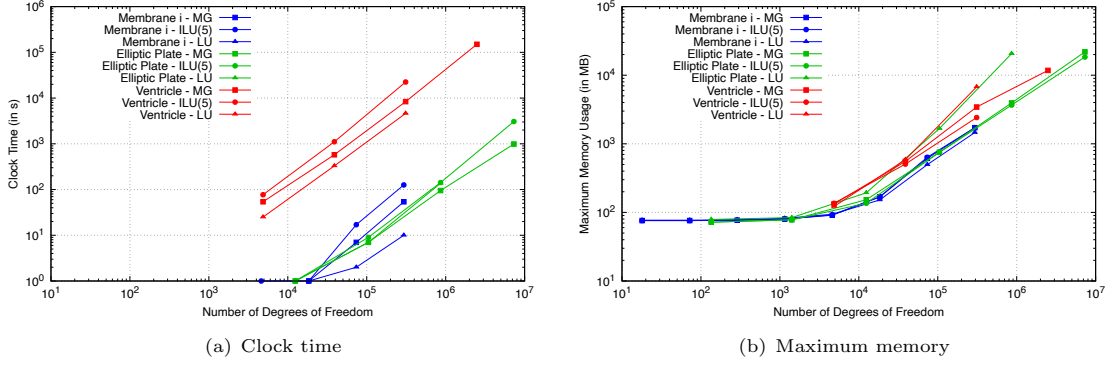


Fig. 22 The clock times and maximum memory usage for three preconditioning approaches (multigrid, ILU(1), and LU) as a function of degrees of freedom

Other linear solver settings: mention these but no need for analyses

In GMRES, we must choose the value of the "restarts" parameter; the default in PETSc of 30 does not always seem good enough (I have been setting it to 100). We could show its affect on one case. I think the optimal choice is linked with the choice of preconditioner (a better preconditioner means we can use a small restart value) so maybe we include this with the "preconditioner choices" section. I suggest we do not add an analysis of this: instead we can just mention it

This can also be considered a linear solver setting. For segregated, we always use a relative tolerance of 0.1, but initial tests for JFNK show that 0.1 is too loose and 1e-3 seems better, although maybe there is no difference with using 1e-6. I suggest we do not add an analysis of this: instead we can just mention it

4.4 Effect of Rhee-Chow Stabilisation

This section highlights the effect of the choice of the global scaling factor α in the Rhee-Chow stabilisation (Equation 25) on the performance of the proposed Jacobian-free Newton Krylov method. As described in Section 2.3, the stabilisation term is introduced to quell zero-energy modes (oscillations) in the discrete solution, such as checkerboarding. As the amount of stabilisation increases (increasing α), these numerical modes are quelled, and the solution stabilises; however, at some point, further increases in the amount of stabilisation reduce the accuracy of the discretisation due to over-smoothing. A less obvious consequence of changing the stabilisation magnitude is its effect on the convergence of the linear solver in the Jacobian-free Newton-Krylov solution procedure. This section examines this effect.

As in the previous section, three cases are used to highlight the effect: membrane i (2-D, linear elastic), elliptic plate (3-D, linear elastic), and idealised ventricle (3-D, hyperelastic). The LU preconditioning method is used for the 2-D membrane i case, while the multigrid approach is used for the two 3-D cases. Figure 23 presents the execution times and the number of accumulated linear solver iterations for three values of global stabilisation factor ($\alpha = [0.01, 0.1, 1]$) for several mesh densities. The memory usage is unaffected by the value of α and is hence not shown.

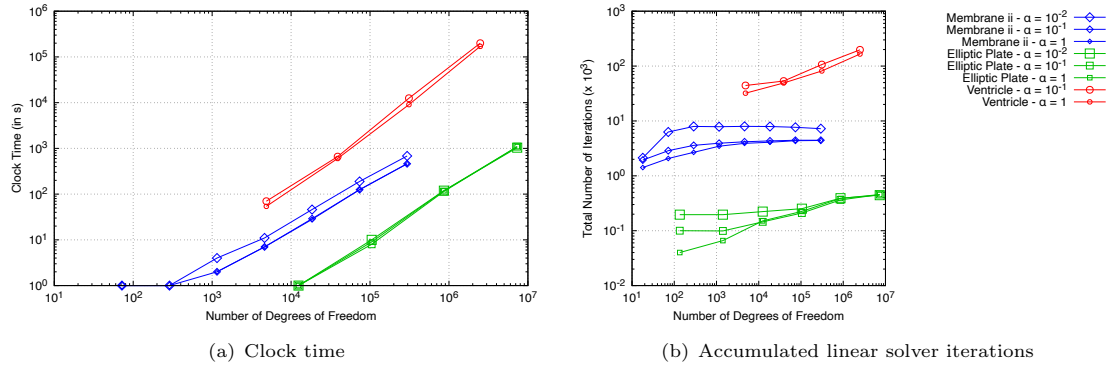


Fig. 23 The clock times and accumulated linear solver iterations for different values of Rhie-Chow global stabilisation factor α

Figure 24 shows a comparison of the stress (or displacement) along the line XXX - ζ we need to show the effect on accuracy for different values of alpha

Fig. 24 Stress predictions along the line XXX for the YYY case using different values of the Rhie-Chow stabilisation factor α

4.5 Parallelisation

In this final analysis, the multi-CPU-core parallel scaling performance of the proposed Jacobian-free Newton Krylov method is examined. Two types of parallel scaling analyses are performed [20]:

- Strong scaling study: Strong scaling measures how the execution time of a fixed problem size (fixed number of cells) decreases as the number of CPU cores increases. Good strong scaling indicates that an application effectively utilises additional CPU cores without significant overhead. In contrast, poor strong scaling suggests that adding more cores does not significantly reduce the execution time, often due to increased communication or synchronisation overhead.
- Weak scaling study: Weak scaling measures how the execution time changes as the problem size (the number of cells) and the number of CPU cores increase proportionally, where the problem

size per CPU core remains (approximately) constant. Good weak scaling indicates that the application can efficiently manage larger workloads with more cores without a significant increase in execution time. Poor weak scaling implies that the application struggles to maintain performance as the problem size and core count increase.

The results from the strong scaling study are shown in Figure 25. The speedup S is defined as $S = t_1/t_p$, where t_1 is the clock time on one CPU core and t_p is the clock time on P CPU cores. In the ideal case, the speedup should double when the number of cores is doubled. In reality, inter-CPU-core communication reduces the parallel scaling efficiency below the ideal. **Comment on the results: e.g. fastest, slowest, most/least iterations, best/worst scaling** Provide insights, if any: e.g. why is one faster or slower

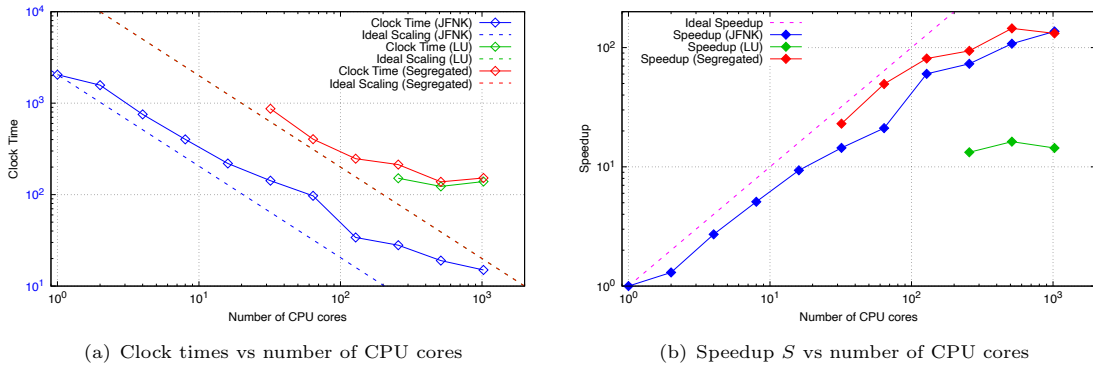


Fig. 25 Strong parallel scaling study comparing the performance of three preconditioning strategies: a LU direct solver, and ILU(N) and multigrid iterative solvers

To run:

- elliptic plate (static, SS): MG, LU, ILU, Seg
- ventricle (dynamic, LS): MG, LU, ILU, Seg

The weak scaling results are shown in Figure 26. The weak scaling efficiency η_w is defined as $\eta_w = t^{[w]_1}/t^{[w]_p}$, where $t^{[w]_1}$ is the clock time on one CPU core and $t^{[w]_p}$ is the clock time on P CPU cores where the problem size per CPU core is constant. In the ideal case, the efficiency should be unity, but inter-CPU-core communication reduces it. **Comment on the results: e.g. fastest, slowest, most/least iterations, best/worst scaling** Provide insights, if any: e.g. why is one faster or slower

placeholder placeholder

(a) Clock times vs number of CPU cores (b) Weak scaling efficiency η_w vs number of CPU cores

Fig. 26 Weak parallel scaling study comparing the performance of three preconditioning strategies: a LU direct solver, and ILU(N) and multigrid iterative solvers

Compare preconditioners

elliptic plate

- mesh 7:
- mesh 8: 18 751 680

5 Conclusions

In the current work, a Jacobian-free Newton-Krylov solution algorithm has been proposed for solid mechanics problems discretised using the cell-centred finite volume method. A compact-stencil discretisation of the diffusion term is proposed as the preconditioner matrix, allowing a straightforward extension of existing segregated solution frameworks. The key findings of the work are:

- Main results
- Main important choices
- How it compares to segregated methods and FE (Abaqus)

Potentially, modifying the compact preconditioner matrix to account for plasticity would allow the method to work in the failed cases, but this will be left for future studies.

Why not use Picard as initial step for JFNK? It is not sufficiently robust: this can be seen in some of the test cases where it diverges, e.g hyperelastic cases. In other cases, convergence is quick so initialisation is not needed. So Picard could work if made more robust (maybe add pseudo time). Add this comment to the conclusions.

Acknowledgments. This project has received funding from the European Research Council (ERC) under the European Union's Horizon 2020 research and innovation programme (Grant Agreement No. 101088740). Financial support is gratefully acknowledged from the Irish Research Council through the Laureate programme, grant number IRCLA/2017/45, from Bekaert through the University Technology Centre (UTC phases I and II) at UCD (www.ucd.ie/bekaert), from I-Form, funded by Science Foundation Ireland (SFI) Grant Numbers 16/RC/3872 and RC2302_2, co-funded under European Regional Development Fund and by I-Form industry partners, and from NexSys, funded by SFI Grant Number 21/SPP/3756. Additionally, the authors wish to acknowledge the DJEI/DES/SFI/HEA Irish Centre for High-End Computing (ICHEC) for the provision of computational facilities and support (www.ichec.ie), and part of this work has been carried out using the UCD ResearchIT Sonic cluster which was funded by UCD IT Services and the UCD Research Office. **Ivan/Zeljko: add any additional acknowledgements here**

Appendix A Truncation Error Analysis of the Rhie-Chow Stabilisation Term

On a 1-D uniform mesh with spacing Δx and unity areas, the Rhie-Chow term stabilisation term (Equation 25) for centre cell P becomes

$$\begin{aligned}\mathcal{D}_{\text{Rhie-Chow}} &= \sum_{f \in N_f} \alpha \bar{K}_f \left[|\Delta_f| \frac{\mathbf{u}_{N_f} - \mathbf{u}_P}{|\mathbf{d}_f|} - \Delta_f \cdot (\nabla \mathbf{u})_f \right] |\Gamma_f| \\ &= \alpha \bar{K} \left[\frac{\mathbf{u}_E - \mathbf{u}_P}{\Delta x} - (\nabla \mathbf{u})_e \right] + \alpha \bar{K} \left[\frac{\mathbf{u}_W - \mathbf{u}_P}{\Delta x} + (\nabla \mathbf{u})_w \right]\end{aligned}\quad (\text{A1})$$

where E and W indicate the east and west neighbour cell centre values, EE and WW are the far east and west neighbour cell centre values, and e and w indicate east and west face values; α and \bar{K} are assumed uniform. The face gradients are calculated as

$$\begin{aligned}(\nabla \mathbf{u})_e &= \frac{1}{2} [(\nabla \mathbf{u})_P + (\nabla \mathbf{u})_E] \\ (\nabla \mathbf{u})_w &= \frac{1}{2} [(\nabla \mathbf{u})_W + (\nabla \mathbf{u})_P]\end{aligned}\quad (\text{A2})$$

where the cell centre gradients are calculated as

$$\begin{aligned}(\nabla \mathbf{u})_W &= \frac{\mathbf{u}_P - \mathbf{u}_{WW}}{2\Delta x} \\ (\nabla \mathbf{u})_P &= \frac{\mathbf{u}_E - \mathbf{u}_W}{2\Delta x} \\ (\nabla \mathbf{u})_E &= \frac{\mathbf{u}_{EE} - \mathbf{u}_P}{2\Delta x}\end{aligned}\quad (\text{A3})$$

The final Rhie-Chow term becomes

$$\begin{aligned}\mathcal{D}_{\text{Rhie-Chow}} &= \alpha \bar{K} \left\{ \frac{\mathbf{u}_E - \mathbf{u}_P}{\Delta x} - \frac{1}{2} [(\nabla \mathbf{u})_P + (\nabla \mathbf{u})_E] + \frac{\mathbf{u}_W - \mathbf{u}_P}{\Delta x} + \frac{1}{2} [(\nabla \mathbf{u})_W + (\nabla \mathbf{u})_P] \right\} \\ &= \alpha \bar{K} \left\{ \frac{\mathbf{u}_E - \mathbf{u}_P}{\Delta x} - \frac{1}{2} (\nabla \mathbf{u})_E + \frac{\mathbf{u}_W - \mathbf{u}_P}{\Delta x} + \frac{1}{2} (\nabla \mathbf{u})_W \right\} \\ &= \alpha \bar{K} \left[\frac{\mathbf{u}_E - \mathbf{u}_P}{\Delta x} - \frac{\mathbf{u}_{EE} - \mathbf{u}_P}{4\Delta x} + \frac{\mathbf{u}_W - \mathbf{u}_P}{\Delta x} + \frac{\mathbf{u}_P - \mathbf{u}_{WW}}{4\Delta x} \right] \\ &= \frac{\alpha \bar{K}}{4\Delta x} [-\mathbf{u}_{WW} + 4\mathbf{u}_W - 6\mathbf{u}_P + 4\mathbf{u}_E - \mathbf{u}_{EE}]\end{aligned}\quad (\text{A4})$$

A local truncation analysis can be performed using the following truncated Taylor series about the true solution (\mathbf{U}) and its gradients $((\nabla \mathbf{U})_P, (\nabla^2 \mathbf{U})_P, \dots)$ at P :

$$\begin{aligned}\mathbf{u}_{WW} &= \mathbf{U}_P - 2\Delta x (\nabla \mathbf{U})_P + \frac{4\Delta x^2}{2!} (\nabla^2 \mathbf{U})_P - \frac{8\Delta x^3}{3!} (\nabla^3 \mathbf{U})_P + O(\Delta x^4) \\ \mathbf{u}_W &= \mathbf{U}_P - \Delta x (\nabla \mathbf{U})_P + \frac{\Delta x^2}{2!} (\nabla^2 \mathbf{U})_P - \frac{\Delta x^3}{3!} (\nabla^3 \mathbf{U})_P + O(\Delta x^4)\end{aligned}$$

$$\begin{aligned}
\mathbf{u}_P &= \mathbf{U}_P \\
\mathbf{u}_E &= \mathbf{U}_P + \Delta x (\nabla \mathbf{U})_P + \frac{\Delta x^2}{2!} (\nabla^2 \mathbf{U})_P + \frac{\Delta x^3}{3!} (\nabla^3 \mathbf{U})_P + O(\Delta x^4) \\
\mathbf{u}_{EE} &= \mathbf{U}_P + 2\Delta x (\nabla \mathbf{U})_P + \frac{4\Delta x^2}{2!} (\nabla^2 \mathbf{U})_P + \frac{8\Delta x^3}{3!} (\nabla^3 \mathbf{U})_P + O(\Delta x^4)
\end{aligned} \tag{A5}$$

where $O(\Delta x^4)$ are higher-order terms with a leading term proportional to Δx^4 .

Substituting the expressions above (Equations A5) for the true solution into Equation A4 results in

$$\begin{aligned}
\mathcal{D}_{\text{Rhee-Chow}} &= \frac{\alpha \bar{K}}{4\Delta x} [-\mathbf{u}_{WW} + 4\mathbf{u}_W - 6\mathbf{u}_P + 4\mathbf{u}_E - \mathbf{u}_{EE}] \\
&= \frac{\alpha \bar{K}}{4\Delta x} \left[-\mathbf{U}_P + 2\Delta x (\nabla \mathbf{U})_P - 4\frac{\Delta x^2}{2!} (\nabla^2 \mathbf{U})_P + 8\frac{\Delta x^3}{3!} (\nabla^3 \mathbf{U})_P \right. \\
&\quad + 4\mathbf{U}_P - 4\Delta x (\nabla \mathbf{U})_P + 4\frac{\Delta x^2}{2!} (\nabla^2 \mathbf{U})_P - 4\frac{\Delta x^3}{3!} (\nabla^3 \mathbf{U})_P \\
&\quad - 6\mathbf{U}_P \\
&\quad + 4\mathbf{U}_P + 4\Delta x (\nabla \mathbf{U})_P + 4\frac{\Delta x^2}{2!} (\nabla^2 \mathbf{U})_P + 4\frac{\Delta x^3}{3!} (\nabla^3 \mathbf{U})_P \\
&\quad \left. - \mathbf{U}_P - 2\Delta x (\nabla \mathbf{U})_P - 4\frac{\Delta x^2}{2!} (\nabla^2 \mathbf{U})_P + 8\frac{\Delta x^3}{3!} (\nabla^3 \mathbf{U})_P + O(\Delta x^4) \right] \\
&= \frac{\alpha \bar{K}}{4\Delta x} \left[16\frac{\Delta x^3}{3!} (\nabla^3 \mathbf{U})_P + O(\Delta x^4) \right] \\
&= \frac{2}{3}\alpha \bar{K} \Delta x^2 (\nabla^3 \mathbf{U})_P + O(\Delta x^3)
\end{aligned} \tag{A6}$$

The leading truncation error is proportional to Δx^2 ! Did I make a mistake...?

Appendix B Body Force for the Method of Manufactured Solutions Case

The body force for the manufactured solution case is

$$\mathbf{f}_b = \begin{cases} \lambda [8a_y\pi^2 \cos(4\pi x) \cos(2\pi y) \sin(\pi z) \\ + 4a_z\pi^2 \cos(4\pi x) \cos(\pi z) \sin(2\pi y) \\ - 16a_x\pi^2 \sin(4\pi x) \sin(2\pi y) \sin(\pi z)] \\ + \mu [8a_y\pi^2 \cos(4\pi x) \cos(2\pi y) \sin(\pi z) \\ + 4a_z\pi^2 \cos(4\pi x) \cos(\pi z) \sin(2\pi y) \\ - 5a_x\pi^2 \sin(4\pi x) \sin(2\pi y) \sin(\pi z)] \\ - 32a_x\mu_\pi^2 \sin(4\pi x) \sin(2\pi y) \sin(\pi z) \\ \\ \lambda [8a_x\pi^2 \cos(4\pi x) \cos(2\pi y) \sin(\pi z) \\ + 2a_z\pi^2 \cos(2\pi y) \cos(\pi z) \sin(4\pi x) \\ - 4a_y\pi^2 \sin(4\pi x) \sin(2\pi y) \sin(\pi z)] \\ + \mu [8a_x\pi^2 \cos(4\pi x) \cos(2\pi y) \sin(\pi z) \\ + 2a_z\pi^2 \cos(2\pi y) \cos(\pi z) \sin(4\pi x) \\ - 17a_y\pi^2 \sin(4\pi x) \sin(2\pi y) \sin(\pi z)] \\ - 8a_y\mu_\pi^2 \sin(4\pi x) \sin(2\pi y) \sin(\pi z) \\ \\ \lambda [4a_x\pi^2 \cos(4\pi x) \cos(\pi z) \sin(2\pi y) \\ + 2a_y\pi^2 \cos(2\pi y) \cos(\pi z) \sin(4\pi x) \\ - a_z\pi^2 \sin(4\pi x) \sin(2\pi y) \sin(\pi z)] \\ + \mu [4a_x\pi^2 \cos(4\pi x) \cos(\pi z) \sin(2\pi y) \\ + 2a_y\pi^2 \cos(2\pi y) \cos(\pi z) \sin(4\pi x) \\ - 20a_z\pi^2 \sin(4\pi x) \sin(2\pi y) \sin(\pi z)] \\ - 2a_z\mu_\pi^2 \sin(4\pi x) \sin(2\pi y) \sin(\pi z) \end{cases} \quad (B7)$$

where μ and λ are the first and second Lamé parameters, respectively.

Appendix C Analytical Expressions for the Stress and Displacement Distributions around a Spherical Cavity under Uniaxial Tensions

The analytical expressions for the stress distributions around the cavity, first derived by Southwell and Gough [58], are

$$\sigma_{rr} = \frac{T}{14 - 10\nu} \frac{a^3}{R^3} \left[9 - 15\nu - 12 \frac{a^2}{R^2} - \frac{r^2}{R^2} \left(72 - 15\nu - 105 \frac{a^2}{R^2} \right) + 15 \frac{r^4}{R^4} \left(5 - 7 \frac{a^2}{R^2} \right) \right], \quad (C8)$$

$$\sigma_{\theta\theta} = \frac{T}{14 - 10\nu} \frac{a^3}{R^3} \left[9 - 15\nu - 12 \frac{a^2}{R^2} - 15 \frac{r^2}{R^2} \left(1 - 2\nu - \frac{a^2}{R^2} \right) \right], \quad (C9)$$

$$\sigma_{zz} = T \left[1 - \frac{1}{14 - 10\nu} \frac{a^3}{R^3} \left\{ 38 - 10\nu - 24 \frac{a^2}{R^2} - \frac{r^2}{R^2} \left(117 - 15\nu - 120 \frac{a^2}{R^2} \right) + 15 \frac{r^4}{R^4} \left(5 - 7 \frac{a^2}{R^2} \right) \right\} \right], \quad (\text{C10})$$

$$\sigma_{zr} = \frac{T}{14 - 10\nu} \frac{a^3 z r}{R^5} \left[-3(19 - 5\nu) + 60 \frac{a^2}{R^2} + 15 \frac{r^2}{R^2} \left(5 - 7 \frac{a^2}{R^2} \right) \right]. \quad (\text{C11})$$

where a is the hole radius, T is the distant stress applied in the z direction, ν is the Poisson's ratio, $r^2 = x^2 + y^2$ is the cylindrical radial coordinate, $R^2 = r^2 + z^2$ is the spherical radial coordinate, and x, y, z are the Cartesian coordinates.

The displacement distributions were later derived by Goodier [59]:

$$u_r = -\frac{A}{r^2} - \frac{3B}{r^4} + \left[\frac{5 - 4\nu}{1 - 2\nu} \frac{C}{r^2} - 9 \frac{B}{r^4} \right] \cos(2\theta), \quad (\text{C12})$$

$$u_\theta = - \left[\frac{2C}{r^2} + 6 \frac{B}{r^4} \right] \sin(2\theta), \quad (\text{C13})$$

where the constants A, B and C are defined as follows:

$$\frac{A}{a^3} = -\frac{T}{8\mu} \frac{13 - 10\nu}{7 - 5\nu}, \quad \frac{B}{a^5} = -\frac{T}{8\mu} \frac{1}{7 - 5\nu}, \quad \frac{C}{a^3} = -\frac{T}{8\mu} \frac{5(1 - 2\nu)}{7 - 5\nu}. \quad (\text{C14})$$

and μ is the shear modulus.

References

- [1] Trangenstein, J.A., Colella, P.: A higher-order Godunov method for modeling finite deformation in elastic-plastic solids. *Communications on Pure and Applied Mathematics* **44**, 41–100 (1991)
- [2] Kluth, G., Després, B.: Discretization of hyperelasticity on unstructured mesh with a cell-centered Lagrangian scheme. *Journal of Computational Physics* **229**, 9092–9118 (2010)
- [3] Lee, C.H., Gil, A.J., Bonet, J.: Development of a cell centred upwind finite volume algorithm for a new conservation law formulation in structural dynamics. *Computers & Structures* **118**, 13–38 (2013)
- [4] Haider, J., Lee, C.H., Gil, A.J., Bonet, J.: A first order hyperbolic framework for large strain computational solid dynamics: An upwind cell centred total Lagrangian scheme. *International Journal for Numerical Methods in Engineering* **109**, 407–456 (2017)
- [5] Demirdžić, I., Martinović, D., Ivanković, A.: Numerical simulation of thermal deformation in welded workpiece. *Zavarivanje* **31**, 209–219 (1988). In Croatian. English translation available at https://www.researchgate.net/profile/Alojz_Ivankovic/publication/296148474_Numerical_simulation_of_thermal_deformation_in_welded_workpiece/links/5d07642ba6fdcc39f12219eb/Numerical-simulation-of-thermal-deformation-in-welded-workpiece.pdf
- [6] Fryer, Y.D., Bailey, C., Cross, M., Lai, C.-H.: A control volume procedure for solving the elastic stress-strain equations on an unstructured mesh. *Applied Mathematical Modelling* **15**,

639–645 (1991)

- [7] Demirdžić, I., Muzaferija, S.: Numerical method for coupled fluid flow, heat transfer and stress analysis using unstructured moving meshes with cells of arbitrary topology. *Computer Methods in Applied Mechanics and Engineering* **125**(1), 235–255 (1995) [https://doi.org/10.1016/0045-7825\(95\)00800-G](https://doi.org/10.1016/0045-7825(95)00800-G)
- [8] Jasak, H., Weller, H.G.: Application of the finite volume method and unstructured meshes to linear elasticity. *International Journal for Numerical Methods in Engineering* **48**(2), 267–287 (2000) [https://doi.org/10.1002/\(SICI\)1097-0207\(20000520\)48:2<267::AID-NME884>3.0.CO;2-Q](https://doi.org/10.1002/(SICI)1097-0207(20000520)48:2<267::AID-NME884>3.0.CO;2-Q) <https://onlinelibrary.wiley.com/doi/pdf/10.1002/%28SICI%291097-0207%2820000520%2948%3A2%3C267%3A%3AAID-NME884%3E3.0.CO%3B2-Q>
- [9] Tuković, Ivanković, A., Karač, A.: Finite-volume stress analysis in multi-material linear elastic body. *International Journal for Numerical Methods in Engineering* **93**(4), 400–419 (2013) <https://doi.org/10.1002/nme.4390> <https://onlinelibrary.wiley.com/doi/pdf/10.1002/nme.4390>
- [10] Cardiff, P., Tuković, Ž., Jaeger, P.D., Clancy, M., Ivanković, A.: A Lagrangian cell-centred finite volume method for metal forming simulation. *International Journal for Numerical Methods in Engineering* **109**(13), 1777–1803 (2017) <https://doi.org/10.1002/nme.5345> <https://onlinelibrary.wiley.com/doi/pdf/10.1002/nme.5345>
- [11] Tuković, Karač, A., Cardiff, P., Jasak, H., Ivanković, A.: Openfoam finite volume solver for fluid-solid interaction. *Transactions of FAMENA* **42**(3), 1–31 (2018) <https://doi.org/10.21278/TOF.42301>
- [12] Batistić, I., Cardiff, P., Tuković, Ž.: A finite volume penalty based segment-to-segment method for frictional contact problems. *Applied Mathematical Modelling* **101**, 673–693 (2022) <https://doi.org/10.1016/j.apm.2021.09.009>
- [13] Das, S., Mathur, S.R., Murthy, J.Y.: An Unstructured Finite-Volume Method for Structure-Electrostatics Interactions in MEMS. *Numerical Heat Transfer, Part B: Fundamentals* **60**(6), 425–451 (2011) <https://doi.org/10.1080/10407790.2011.628252> <https://doi.org/10.1080/10407790.2011.628252>
- [14] Cardiff, P., Tuković, Ž., Jasak, H., Ivanković, A.: A block-coupled finite volume methodology for linear elasticity and unstructured meshes. *Computers & Structures* **175**, 100–122 (2016) <https://doi.org/10.1016/j.compstruc.2016.07.004>
- [15] Castrillo, P., Schillaci, E., Rigola, J.: High-order cell-centered finite volume method for solid dynamics on unstructured meshes. *Computers & Structures* **295**, 107288 (2024) <https://doi.org/10.1016/j.compstruc.2024.107288>
- [16] McHugh, P.R., Knoll, D.A.: Comparison of standard and matrix-free implementations of several newton-krylov solvers. *AIAA Journal* **32**(12), 2394–2400 (1994) <https://doi.org/10.2514/3.12305>
- [17] Qin, N., Ludlow, D.K., Shaw, S.T.: A matrix-free preconditioned newton/gmres method

- for unsteady navier–stokes solutions. International Journal for Numerical Methods in Fluids **33**(2), 223–248 (2000) [https://doi.org/10.1002/\(SICI\)1097-0363\(20000530\)33:2<223::AID-FLD10>3.0.CO;2-V](https://doi.org/10.1002/(SICI)1097-0363(20000530)33:2<223::AID-FLD10>3.0.CO;2-V)
- [18] Geuzaine, P.: Newton-krylov strategy for compressible turbulent flows on unstructured meshes. AIAA Journal **39**(3), 528–531 (2001) <https://doi.org/10.2514/2.1339>
 - [19] Pernice, M., Tocci, M.D.: A multigrid-preconditioned newton–krylov method for the incompressible navier–stokes equations. SIAM Journal on Scientific Computing **23**(2), 398–418 (2001) <https://doi.org/10.1137/S1064827500372250>
 - [20] Knoll, D.A., Keyes, D.E.: Jacobian-free newton–krylov methods: a survey of approaches and applications. Journal of Computational Physics **193**(2), 357–397 (2004) <https://doi.org/10.1016/j.jcp.2003.08.010>
 - [21] Nejat, A., Ollivier-Gooch, C.: A high-order accurate unstructured finite volume newton–krylov algorithm for inviscid compressible flows. Journal of Computational Physics **227**(4), 2582–2609 (2008) <https://doi.org/10.1016/j.jcp.2007.11.011>
 - [22] Vaassen, J.-M., Vigneron, D., Essers, J.-A.: An implicit high order finite volume scheme for the solution of 3d navier–stokes equations with new discretization of diffusive terms. Journal of Computational and Applied Mathematics **215**(2), 595–601 (2008) <https://doi.org/10.1016/j.cam.2006.04.066>
 - [23] Lucas, P., Zuijlen, A.H., Bijl, H.: Fast unsteady flow computations with a jacobian-free newton–krylov algorithm. Journal of Computational Physics **229**(24), 9201–9215 (2010) <https://doi.org/10.1016/j.jcp.2010.08.033>
 - [24] Nejat, A., Jalali, A., Sharbatdar, M.: A newton–krylov finite volume algorithm for the power-law non-newtonian fluid flow using pseudo-compressibility technique. Journal of Non-Newtonian Fluid Mechanics **166**(19–20), 1158–1172 (2011) <https://doi.org/10.1016/j.jnnfm.2011.07.003>
 - [25] Nishikawa, H.: A hyperbolic poisson solver for tetrahedral grids. Journal of Computational Physics **409**, 109358 (2020) <https://doi.org/10.1016/j.jcp.2020.109358>
 - [26] Gear, C.W., Saad, Y.: Iterative solution of linear equations in ode codes. SIAM Journal on Scientific and Statistical Computing **4**(4), 583–601 (1983) <https://doi.org/10.1137/0904040>
 - [27] Chan, T.F., Jackson, K.R.: Nonlinearly preconditioned krylov subspace methods for discrete newton algorithms. SIAM Journal on Scientific and Statistical Computing **5**(3), 533–542 (1984) <https://doi.org/10.1137/0905039>
 - [28] Brown, P.N., Hindmarsh, A.C.: Matrix-free methods for stiff systems of ode's. SIAM Journal on Numerical Analysis **23**(3), 610–638 (1986) <https://doi.org/10.1137/0723034>
 - [29] Brown, P.N., Saad, Y.: Hybrid krylov methods for nonlinear systems of equations. SIAM Journal on Scientific and Statistical Computing **11**(3), 450–481 (1990) <https://doi.org/10.1137/0911026>

- [30] Badcock, K.J., Gaitonde, A.L.: An unfactored implicit moving mesh method for the two-dimensional unsteady n-s equations. International Journal for Numerical Methods in Fluids **23**(6), 607–631 (1996) [https://doi.org/10.1002/\(SICI\)1097-0363\(19960930\)23:6<607::AID-FLD433>3.0.CO;2-E](https://doi.org/10.1002/(SICI)1097-0363(19960930)23:6<607::AID-FLD433>3.0.CO;2-E). First published: 30 September 1996
- [31] Balay, S., Abhyankar, S., Adams, M.F., Brown, J., Brune, P., Buschelman, K., Dalcin, L., Eijkhout, V., Gropp, W.D., Kaushik, D., Knepley, M.G., McInnes, L.C., Rupp, K., Smith, B.F., Zampini, S., Zhang, H.: PETSc Web page. <http://www.mcs.anl.gov/petsc> (2015). <http://www.mcs.anl.gov/petsc>
- [32] Nishikawa, H., Nakashima, Y., Watanabe, N.: Effects of high-frequency damping on iterative convergence of implicit viscous solver. Journal of Computational Physics **348**, 66–81 (2017) <https://doi.org/10.1016/j.jcp.2017.07.021>
- [33] Weller, H.G., Tabor, G., Jasak, H., Fureby, C.: A tensorial approach to computational continuum mechanics using object orientated techniques. Computers in Physics **12**, 620–631 (1998)
- [34] Rhie, C.M., Chow, W.L.: Numerical study of the turbulent flow past an airfoil with trailing edge separation. AIAA Journal **21**(11), 1525–1532 (1983) <https://doi.org/10.2514/3.8284> <https://doi.org/10.2514/3.8284>
- [35] Cardiff, P., Karac, A., Jaeger, P.D., Jasak, H., Nagy, J., Ivanković, A., Tuković: An open-source finite volume toolbox for solid mechanics and fluid-solid interaction simulations (2018) <https://doi.org/10.48550/arXiv.1808.10736> . <https://arxiv.org/abs/1808.10736>
- [36] Jasak, H.: Error analysis and estimation for the finite volume method with applications to fluid flows. PhD thesis, Imperial College London (University of London) (1996)
- [37] Jsvobs, D.A.H.: A Generalization of the Conjugate-Gradient Method to Solve Complex Systems. IMA Journal of Numerical Analysis **6**(4), 447–452 (1986) <https://doi.org/10.1093/imanum/6.4.447> <https://academic.oup.com/imajna/article-pdf/6/4/447/2181350/6-4-447.pdf>
- [38] Falgout, R.D., Yang, U.M.: hypre: A library of high performance preconditioners. In: Sloot, P.M.A., Hoekstra, A.G., Tan, C.J.K., Dongarra, J.J. (eds.) Computational Science — ICCS 2002, pp. 632–641. Springer, Berlin, Heidelberg (2002)
- [39] Amestoy, P.R., Duff, I.S., Koster, J., L'Excellent, J.-Y.: A fully asynchronous multi-frontal solver using distributed dynamic scheduling. SIAM Journal on Matrix Analysis and Applications **23**(1), 15–41 (2001)
- [40] Amestoy, P.R., Buttari, A., L'Excellent, J.-Y., Mary, T.: Performance and Scalability of the Block Low-Rank Multifrontal Factorization on Multicore Architectures. ACM Transactions on Mathematical Software **45**, 2–1226 (2019)
- [41] Geuzaine, C., Remacle, J.-F.: Gmsh: A 3-d finite element mesh generator with built-in pre- and post-processing facilities. International journal for numerical methods in engineering **79**(11), 1309–1331 (2009) <https://doi.org/10.1002/nme.2579>

- [42] Hitchings, D., Davies, G.A.O., Kamoulakos, A.: Linear Static Benchmarks. International Association for the Engineering Analysis Community & National Agency for Finite Element Methods & Standards (NAFEMS), Glasgow, UK (1987)
- [43] Demirdžić, I., Muzaferija, S., Perić, M.: Advances in computation of heat transfer, fluid flow, and solid body deformation using finite volume approaches. In: W. J. Minkowycz, E.M.S. (ed.) *Advances in Numerical Heat Transfer*, Chapter 2, pp. 59–96. Taylor & Francis, ??? (1997)
- [44] Cardiff, P., Tuković, Jasak, H., Ivanković, A.: A block-coupled finite volume methodology for linear elasticity and unstructured meshes. *Computers & Structures* **175**, 100–122 (2016) <https://doi.org/10.1016/j.compstruc.2016.07.004>
- [45] Rohatgi, A.: WebPlotDigitizer. <https://automeris.io>
- [46] Land, S., Gurev, V., Arens, S., Augustin, C.M., Baron, L., Blake, R., Bradley, C., Castro, S., Crozier, A., Favino, M., Fastl, T.E., Fritz, T., Gao, H., Gizzi, A., Griffith, B.E., Hurtado, D.E., Krause, R., Luo, X., Nash, M.P., Pezzuto, S., Plank, G., Rossi, S., Ruprecht, D., Seemann, G., Smith, N.P., Sundnes, J., Rice, J.J., Trayanova, N., Wang, D., Wang, Z.J., Niederer, S.A.: Verification of cardiac mechanics software: benchmark problems and solutions for testing active and passive material behaviour **471**(2184), 20150641 (2015) <https://doi.org/10.1098/rspa.2015.0641>
- [47] Guccione, J.M., Costa, K.D., McCulloch, A.D.: Finite element stress analysis of left ventricular mechanics in the beating dog heart. *Journal of Biomechanics* **28**(10), 1167–1177 (1995) [https://doi.org/10.1016/0021-9290\(94\)00174-3](https://doi.org/10.1016/0021-9290(94)00174-3)
- [48] Zienkiewicz, O.C., Taylor, R.L.: The Finite Element Method vol. 2. Butterworth-heinemann, ??? (2000)
- [49] Areias, P.: Simplas. Portuguese Software Association (ASSOFT). <http://www.simplassoftware.com>.
- [50] Pelteret, J.-P., McBride, A.: The deal.II code gallery: Quasi-Static Finite-Strain Compressible Elasticity. Zenodo (2018). <https://doi.org/10.5281/zenodo.1228964> . <https://doi.org/10.5281/zenodo.1228964>
- [51] Simo, J.C., Armero, F.: Geometrically non-linear enhanced strain mixed methods and the method of incompatible modes. *International Journal for Numerical Methods in Engineering* **33**(7), 1413–1449 (1992) <https://doi.org/10.1002/nme.1620330705> <https://onlinelibrary.wiley.com/doi/pdf/10.1002/nme.1620330705>
- [52] Sá, J.M.A., Areias, P.M.A., Natal Jorge, R.M.: Quadrilateral elements for the solution of elasto-plastic finite strain problems. *International Journal for Numerical Methods in Engineering* **51**(8), 883–917 (2001) <https://doi.org/10.1002/nme.183> <https://onlinelibrary.wiley.com/doi/pdf/10.1002/nme.183>
- [53] Tuković, Ž., Jasak, H.: Updated lagrangian finite volume solver for large deformation dynamic response of elastic body. *Transactions of FAMENA* **31**(1), 55–70 (2007)

- [54] Turek, S., Hron, J.: Proposal for numerical benchmarking of fluid-structure interaction between an elastic object and laminar incompressible flow. In: Bungartz, H.-J., Schäfer, M. (eds.) Fluid-Structure Interaction: Modelling, Simulation, Optimisation. Lecture Notes in Computational Science and Engineering, vol. 53, pp. 371–385. Springer, Berlin, Heidelberg (2006). https://doi.org/10.1007/3-540-34596-5_20
- [55] Ferziger, J.H., Peric, M.: Computational Methods for Fluid Dynamics, 3rd edn. Springer, ??? (2002)
- [56] Degroote, J., Bathe, K.-J., Vierendeels, J.: Performance of a new partitioned procedure versus a monolithic procedure in fluid-structure interaction. Computers & Structures **87**(11-12), 793–801 (2009) <https://doi.org/10.1016/j.compstruc.2009.01.006>
- [57] Tuković, Ž., Karač, A., Cardiff, P., Jasak, H., Ivanković, A.: OpenFOAM finite volume solver for fluid-solid interaction. Transactions of FAMENA **42**(3), 1–31 (2018) <https://doi.org/10.21278/TOF.42301>
- [58] Southwell, R.V., Gough, H.J.: Vi. on the concentration of stress in the neighbourhood of a small spherical flaw; and on the propagation of fatigue fractures in “statistically isotropic” materials. The London, Edinburgh, and Dublin Philosophical Magazine and Journal of Science **1**(1), 71–97 (1926) <https://doi.org/10.1080/14786442608633614> <https://doi.org/10.1080/14786442608633614>
- [59] Goodier, J.N.: Concentration of stress around spherical and cylindrical inclusions and flaws. Journal of Applied Mechanics **1**(2), 39–44 (1933)